Geol. Mag. **154** (*5*), *2017, pp. 963–982.* © *Cambridge University Press 2016*
doi:10.1017/S0016756816000534

Genesis and implications of the Late Jurassic Hailesitai granites in the northern Greater Khingan Range: evidence from zircon U–Pb dating and Hf isotope

PINGPING ZHU*‡, QIUMING CHENG*‡§, ZHENJIE ZHANG§† & ZIYE WANG‡

*Faculty of Earth Resources, China University of Geosciences, Wuhan 430074, China
‡State Key Laboratory of Geological Process and Mineral Resources, China University of Geosciences, Wuhan 430074, Beijing 100083, China
§School of Earth Sciences and Resources, China University of Geosciences, Beijing 100083, China

(*Received* 17 November 2015; *accepted* 18 May 2016; *first published online* 11 July 2016)

Abstract – The tectonic setting and geodynamic model of the Greater Khingan Range (GKR) is highly controversial due to the lack of reliable geological, isotopic and geochronological evidence. In the current study, the Hailesitai pluton, located at the west of the suture between the northern and southern GKR in the east of the Central Asian Orogenic Belt, is selected to address this issue. These granites of the high potassium calc-alkaline series belong to the A1-type granites with typical geochemical characteristics including high contents of Al_2O_3, extremely low contents of Ti, P, enriched LREE, LILE, depleted HFSE, and a medium Eu negative anomaly. Laser ablation inductively coupled plasma mass spectrometer (LA-ICP-MS) zircon U–Pb dating indicates that the granites can be divided into two stages: *c.* 152 and *c.* 161 Ma. The intrusion of A1-type granites at ~161 Ma implies that intra-plate orogenesis of the northern GKR started at *c.* 161 Ma at latest. The Hailesitai pluton has relatively homogeneous Hf isotope compositions with a ε_{Hf} (t) value (+6.0 – +9.0), and two-stage depleted mantle model ages of 579–738 Ma show that the original magma is a mixture of juvenile and crustal source rocks. Extensional collapse of the Mongol–Okhotsk belt between the Siberia block and the northern GKR resulted in the formation of late Jurassic A1-type granites in the northern GKR. The Hailesitai pluton formed in response to post-orogenic extensional collapse of the Mongol–Okhotsk belt, coupled with back-arc extension related to Palaeo-Pacific plate subduction.

Keywords: northern Greater Khingan Range, Hailesitai pluton, A1-type granite, U–Pb dating, Hf isotope.

1. Introduction

The northern Greater Khingan Range (GKR) is located in the east of the Central Asian Orogenic Belt (CAOB), which is well known for its orogenic characteristics and is the world's largest site of juvenile crustal formation from the Phanerozoic Eon (Jahn, 2004; Wu *et al.* 2011). There are a number of differing hypotheses regarding the evolution of the GKR: (1) a mantle plume (Shao *et al.* 1994; Ge *et al.* 1999; Lin *et al.* 1999), (2) the closure of the northern Mongol–Okhotsk Ocean (i.e. the east of the Palaeo-Asian Ocean) (Guo *et al.* 2001; Wang *et al.* 2002; Fan *et al.* 2003; Meng, 2003), and (3) the subduction of the Palaeo-Pacific Plate (Wang *et al.* 2006; J. Zhang *et al.* 2006, 2008). The focus of controversy is the tectonic setting and timing of the GKR (Wu *et al.* 2007, 2011). This issue might be addressed by the study of A-type (Collins *et al.* 1982; Whalen, Currie & Chappell, 1987; Eby, 1990, 1992; Bonin, 2007; Frost & Frost, 2010), which is the most important part of the alkaline magmatic belt in the GKR (Wu *et al.* 2002; Jahn *et al.* 2009). Wu *et al.* (2002) concluded that the A-type granites in NE China were generated at three different times, involving multiple processes operative in different tectonic environments. The study of Neoproterozoic intrusive rocks in the Erguna Massif of NE China, in the eastern segment of the CAOB, by Tang *et al.* (2013) led to the conclusion that the Neoproterozoic A-type granitoids formed in an extensional environment. However, the petrological evidence provided in previous studies (Wu *et al.* 2005; J. Zhang *et al.* 2008; Lei & Wang, 2011; D. Zhang *et al.* 2015) may not have explained fully the evolution of the GKR, due to the lack of precise geochronological and geochemical data. In this work, the Hailesitai pluton (Fig. 1a, b, c) close to the north of the Hegenshan deep fault was chosen to reveal further the tectonic evolution of the northern GKR in the Late Mesozoic. According to whole rock geochemistry, zircon U–Pb dating and Hf isotope, the aim of this study is to interpret the genesis of the Hailesitai pluton and to provide preliminary evidence supporting the Late Mesozoic tectonic evolution of the northern GKR.

†Author for correspondence: zjzhang@cugb.edu.cn; zzj1117@126.com

2. Geological setting and petrography

The Hailesitai coarse-grained granite pluton is located in the northern GKR (Fig. 1b) and belongs to the East Ujimqin metallogenic belt of the GKR metallogenic

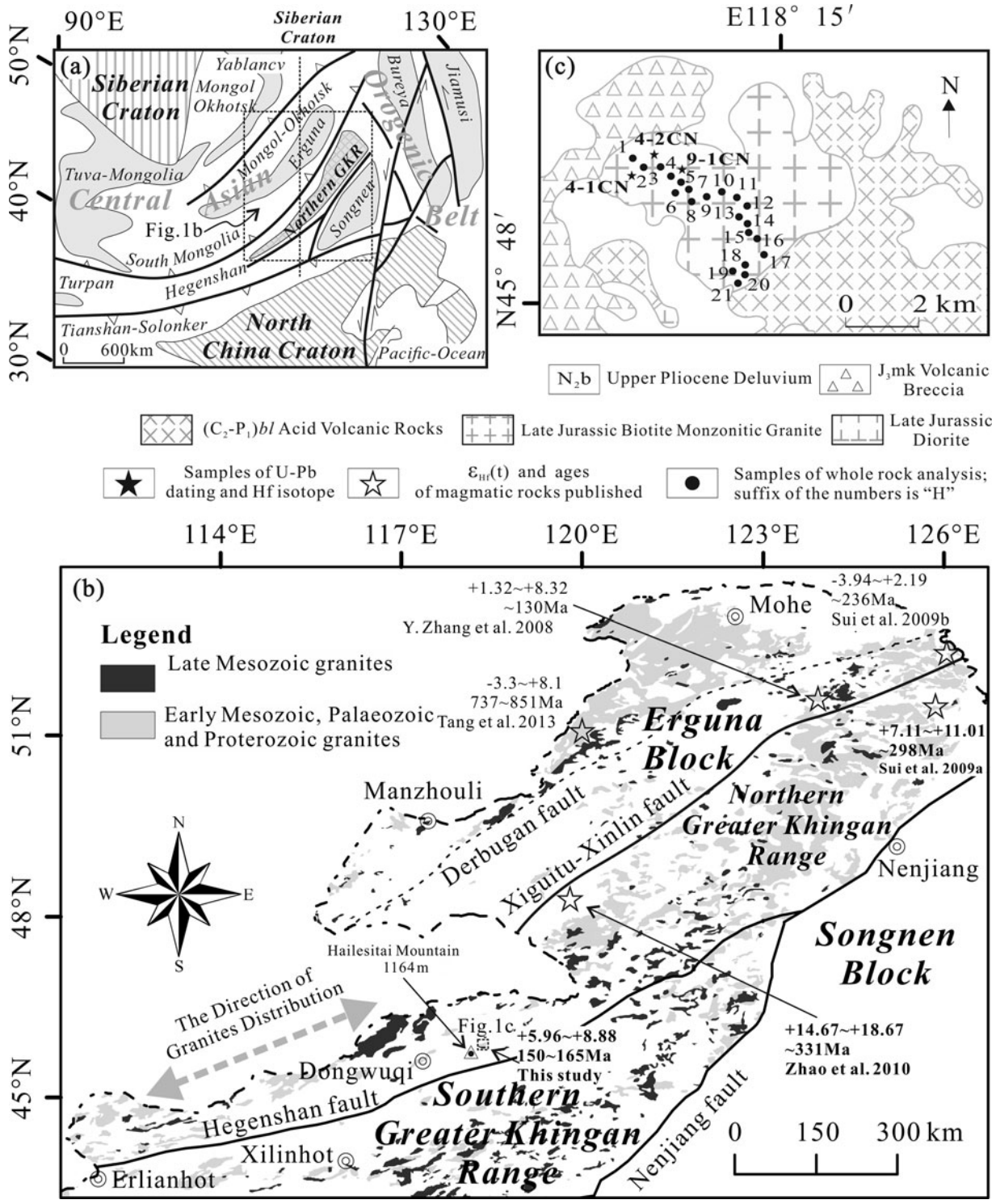

Figure 1. (a) Structural outline sketch of the Central Asian Orogenic Belt (CAOB) (after Zhou *et al*. 2011). The dotted line represents the direction of the profile in Figure 11. (b) The distribution of Phanerozoic granites in the Greater Khingan Range (GKR) and adjacent area (modified from Zhang *et al.* 2013; data cited from Zhang, Ge & Liu, 2008; Sui *et al.* 2009*a*, *b*; Zhao *et al.* 2010; Tang *et al.* 2013). (c) Geological map of Hailesitai pluton (after Zhang *et al.* 2007). (a) is after Zhou *et al.* (2011); the dotted line represents the direction of profile in Figure 11. (b) is modified from Zhang *et al.* (2013) and data cited from Zhang, Ge & Liu (2008), Sui *et al.* (2009*a*, *b*), Zhao *et al.* (2010) and Tang *et al.* (2013). (c) is after Zhang *et al.* (2007).

province within the circum-Pacific metallogenic domain. The strata exposed in the northern GKR are Ordovician, Silurian, Devonian, Permian, Jurassic and Cretaceous volcanic sedimentary rocks and Tertiary and Quaternary sediments (Voo, Spakman & Bijwaard, 1999; Wu *et al.* 2000, 2005; Lin *et al.* 2003). The faults in the northern GKR can be divided into major NE-trending faults, distributed along the fold axis and the two wings, and secondary NW-trending extension faults, which have transformed and damaged

https://doi.org/10.1017/S0016756816000534 Published online by Cambridge University Press

the earlier fractures. The Indosinian (i.e. late Permian – Triassic) and Yanshanian (i.e. Jurassic–Cretaceous) granites, which show some spatial correlation with ore deposits, are widespread in the northern GKR. The Indosinian intrusive rocks, mainly fine-grained biotite granites and coarse-grained granites, have a scattered distribution. In contrast, the evidence of Yanshanian magmatic activity in this region is stronger, and is characterized by high-K alkaline rocks (J. Zhang *et al.* 2006). Spatially, volcanic rocks are often contemporaneous and dominant in the Early Cretaceous, although magmatic activity is generally multi-phase (Zhang *et al.* 2010).

The output strata in the study area comprise the early Ordovician Tongshan Formation (O_1t) with dense dark-brown siltstone, the late Carboniferous–early Permian Baoligaomiao Formation ((C_2–P_1)*bl*) with a series of volcanic rocks including volcanic breccia, rhyolite and dacite, the Late Jurassic Manketouebo Formation (J_3mk) with acid volcanic rocks, and the Pliocene Baogedawula Formation (N_2b) with brick-red clay. The Hailesitai pluton intruded into these lithologies. Two groups of NE- and NW-trending faults are identified, but there is no obvious evidence of altered cataclasites and mylonites. The K-feldspar cluster is widespread at the margins of the pluton. The syenogranite enclaves, which are angular–subangular, are wrapped in the syenogranite with sizes extending from one to tens of centimetres, and alteration and mineralization characteristics are not obvious.

The Hailesitai coarse-grained monzogranitic pluton was named after the Hailesitai Mountain, which lies *c.* 20 km to the NE of the pluton (Fig. 1b). It crops out in an apple shape, *c.* 15 km^2, and the shortest and longest axes are 1 and 6 km, respectively. A large number of quartz veins with widths of a few millimetres to tens of centimetres penetrate the pluton. In addition, some dense dark-brown siltstone fragments of the early Ordovician Tongshan Formation (O_1t) are visible in the pluton. The pluton consists of biotite granite, muscovite granite and two-mica granite. The biotite granite, with massive structure and porphyritic texture, is exposed in the NW of the pluton. It mainly contains K-feldspar (38–42 %), plagioclase (18–34 %), quartz (20–40 %) and biotite (1–8 %), and the accessory minerals consist of apatite, zircon, magnetite and sphene (<1 %). In addition, the widespread biotite granite and rhyolite enclaves, with irregular circular or oval shapes that are one to tens of centimetres in diameter, show a gradual transitional relationship with the host rocks. The muscovite granite crops out in the south of the pluton with massive structure and porphyritic and granitic textures, whereas the two-mica granite is distributed in the middle of the pluton. The muscovite granite is composed of muscovite (1–4 %), whereas, the the two-mica granite is composed of muscovite (1–2 %) and biotite (1–5 %). Both the biotite and muscovite granites show the general granite texture, and phanerocryst is coarse in granularity (Fig. 2a). The perhitic texture of plagioclase (Fig. 2b), amphibole ceramics (Fig. 2c) and the corrosion structure of quartz (Fig. 2d) could be seen frequently under the microscope.

3. Samples and methods

3.a. Samples

Systematic sampling of the coarse-grained granite in the Hailesitai pluton was implemented after detailed field studies. These samples included the biotite and muscovite granites from the NW to the SW of the pluton. The layout of the sampling was generally perpendicular to the change of lithology in order to collect representative samples effectively (Fig. 1c). The samples were fresh enough for geochemical analyses. In the NW of the pluton, three biotite granite whole-rock samples (1H, 2H and 3H) were collected for the analysis of the major and trace elements. Two samples (4–1CN and 4–2CN), which according to their interpenetration relationships belong to different stages, were collected for the zircon U–Pb dating and Hf isotopic analyses. In the middle of the pluton, where the biotite and muscovite granites are distributed, 14 whole-rock samples (from 4H to 7H) were collected for the analysis of major and trace elements, and a muscovite granite sample (9–1CN) was obtained for the zircon U–Pb dating and Hf isotopic analyses. In the SW of the pluton, four muscovite granite whole-rock samples (from 18H to 21H) were collected for the analysis of major and trace elements. The lithology of the muscovite granite in the SW of the pluton is consistent with that in the middle, and there are no features of multiple stages and cross interspersion. The spatial distribution of the samples collected was reasonable and considered to reflect the geochemical characteristics of the coarse-grained granite of the Hailesitai pluton adequately.

3.b. Whole-rock major and trace elements

The whole-rock major, trace and rare-earth element (REE) analyses were conducted at the Analytical Institute of the Hubei Bureau of Geology and Mineral Resources. Major element analyses were conducted using a Regaku 3080E XRF spectrometer. Analytical procedures are described in detail by Gao *et al.* (1995). Trace elements, including REEs, were analysed at the State Key Laboratory of Geological Processes and Mineral Recourses (GPMR), China University of Geosciences, Wuhan, using an Agilent 7500a inductively coupled plasma mass spectrometer (ICP-MS). The analytical procedures are reported in detail by Liu *et al* (2008). Analytical precision (two standard deviations) estimated from repeated analyses of three standard reference samples G-2, AGV-1 and GSR-3 is better than 5 % for REEs and 5–12 % for other trace elements.

3.c. Zircon U–Pb dating

The zircon grains were separated after the rock was crushed using conventional techniques (i.e. heavy

https://doi.org/10.1017/S0016756816000534 Published online by Cambridge University Press

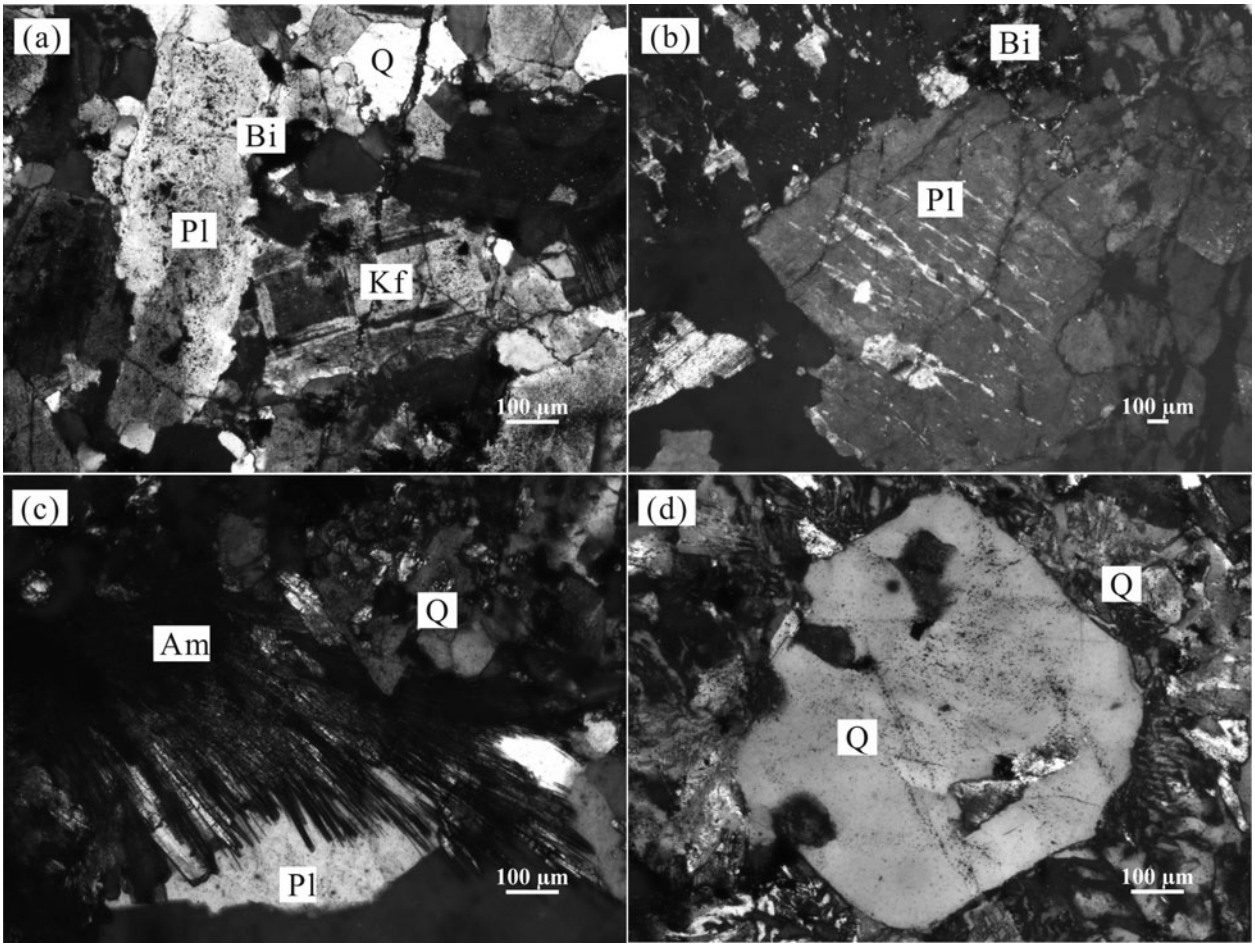

Figure 2. Microscope photographs of Hailesitai pluton: (a) typical structure of granite; (b) perthitic texture of plagioclase; (c) amphibole ceramics; (d) corrosion structure of quartz. Q, quartz; Kf, potassium-feldspar; Pl, plagioclase; Bi, biotite; Am, amphibole.

liquid and magnetic properties). They were then selected by examination using a binocular microscope, mounted in epoxy resin, and polished to approximately half exhumation. Finally, cathodoluminescence images were taken, which were used to study the internal structures of individual zircon grains and as a guide for *in situ* U−Pb dating and Hf isotope analysis. Zircon U−Pb dating was conducted using an ICP-MS (Neptune) coupled with a laser ablation (LA) system using a GeoLas 2005 DUV 193-nm UArF laser at the GPMR. A 32 μm spot size was adopted in this study, with a laser repetition rate of 10 Hz and energy up to 90 mJ. Helium was used as a carrier gas to enhance the transport efficiency of ablated material. The procedure applied is described in detail by Liu *et al.* (2010). Zircon 91500 were used as external standards for the U/Pb ratio. A common lead correction was performed after the method of Andersen (2002), and the isotopic ratios and element concentrations were calculated using ICPMSDataCal8.9 (Liu *et al.* 2010). Data-point uncertainties are 1σ at a confidence interval of 95 %. The method for recalculating the LA-ICP-MS age uncertainties is reported by Horstwood *et al.* (2016). The concordia diagrams and U−Pb ages were obtained using the Isoplot program (Ludwig, 2009).

3.d. Zircon Hf isotope

The Zircon Hf isotope analyses were performed using an excimer laser ablation system (193 nm, ArF) attached to a Neptune multicollector MC-ICP-MS at the GPMR. A laser repetition rate of 10 Hz at 100 mJ was used for ablating the zircon. The spot diameter was 44 μm, and the time of laser-ablation was 26 s. The detailed analytical technique is described by Yuan *et al.* (2008). The standard $^{176}Hf/^{177}Hf$ ratio of zircon 91500 obtained during the analyses was 0.282299 ± 17 (2σ, $n = 38$), which is consistent with the solution-method measurement (0.282306 ± 9) of Woodhead *et al.* (2004). The correction factor is 0.46–0.03 %, and uncertainty in the preferred values for zircon 91500 was propagated to the ultimate results for the samples according to Liu *et al.* (2010). The $^{179}Hf/^{177}Hf$ and $^{173}Yb/^{171}Yb$ ratios were used to calculate the mass bias of Hf (β_{Hf}) and Yb (β_{Yb}), which were normalized to $^{179}Hf/^{177}Hf = 0.7325$ and $^{173}Yb/^{171}Yb = 1.132685$ (Fisher, Vervoort & Hanchar, 2014) using an exponential correction for mass bias. Interference of ^{176}Yb on ^{176}Hf was corrected by measuring the interference-free ^{173}Yb isotope and using $^{176}Yb/^{173}Yb = 0.79639$ (Fisher, Vervoort & Hanchar, 2014) to calculate $^{176}Yb/^{177}Hf$.

https://doi.org/10.1017/S0016756816000534 Published online by Cambridge University Press

Similarly, the relatively minor interference of ^{176}Lu on ^{176}Hf was corrected by measuring the intensity of the interference-free ^{175}Lu isotope and using the recommended $^{176}Lu/^{175}Lu = 0.02656$ (Blichert-Toft, Chauvel & Albarède, 1997) to calculate $^{176}Lu/^{177}Hf$. We used the mass bias of Yb (β_{Yb}) to calculate the mass fractionation of Lu because of their similar physicochemical properties. Offline selection and integration of analyte signals, and mass bias calibrations were performed using ICPMSDataCal (Liu *et al.* 2010). Initial $^{176}Hf/^{177}Hf$ ratios, denoted as ε_{Hf} (t), are calculated relative to a chondritic reservoir with a $^{176}Hf/^{177}Hf$ ratio of 0.282772 and $^{176}Lu/^{177}Hf$ of 0.0332 (Blichert-Toft, Chauvel & Albarède, 1997). The decay constant value of 1.865×10^{-11} a^{-1} for ^{176}Lu reported by Scherer, Munker & Mezger (2001) and an fcc (continental crust) value of −0.55 (Griffin *et al.* 2000) for calculation of two-stage model age were used.

4. Results

4.a. Whole-rock major and trace elements

The results of the analyses of the whole-rock major and trace element contents of selected samples from the Hailesitai pluton are summarized in Table 1. The selected 21 samples show high contents of SiO_2 varying from 74.53 to 77.23 wt % (average 75.50 wt %) (Table 1). The high K_2O contents (4.49−5.57 wt %; average 4.78 wt %) and the high $K_2O + Na_2O$ values (8.25−9.00 wt %; average 8.45 wt %) show the high alkali nature of the granites. The Al_2O_3 contents varying from 12.12 to 13.74 wt % with an average of 12.42 wt % indicate that the granites are rich in aluminium. Furthermore, ASI (Aluminium Saturation Index) is from 1.0 to 1.3 (average 1.1), which suggests that Hailesitai granites are peraluminous (Table 1). The MgO contents are within the range 0.14–0.35 wt %, which is similar to the FeO and Fe_2O_3 contents (0.12–0.32 wt % and 0.35–1.17 wt %). The Fe∗ (Fe∗ = $FeO^{tot}/(FeO^{tot} + MgO)$) ratios vary within the range 0.69−0.91 wt % (average 0.78 wt %). The CaO contents range from 0.17 to 0.63 wt % (average 0.36 wt %), and the TiO_2 contents range from 0.09 to 0.29 wt % with an average of 0.26 wt %. The values from the Litman index ($\delta = (K_2O + Na_2O)^2/SiO_2 - 43$) (2.03−2.46; average 2.19) of these samples show typical characteristics of calc-alkaline granites. The REE and trace element contents of the samples from the Hailesitai pluton are listed in Table 1. In diagrams of SiO_2 versus Fe∗ (Molecular) and SiO_2 versus MALI (Modified Alkali-Lime Index) (Frost *et al.* 2001), the Hailesitai granites show geochemical characteristics of calcic-alkali and transitional ferroan (Fig. 3a, b). The total REE contents of the biotite and muscovite granites (Table 1) range from 89.87 to 214.14 ppm (average 154.35 ppm) and 121.95–202.51 ppm (average 158.78 ppm), respectively. The Chondrite-normalized REE patterns exhibit similar characteristics between the biotite and muscovite granites in the Hailesitai pluton (Fig. 4a). They are both enriched in light REEs and relatively depleted in heavy REEs; both have a right-deviation Chondrite-normalized pattern with a light-to-heavy REE ratio of 15.16−25.46 (average 19.55) and 16.24−23.23 (average 19.47) and La_N/Yb_N ratios of 13.77−29.44 (average 21.38) and 17.52−22.89 (average 20.35), respectively. All samples show an obvious negative Eu anomaly. The trace element spider diagrams of the biotite and muscovite granites (Fig. 4b) are consistent. The contents of Rb, Th, U, K, Zr, Hf and other large-ion lithophile elements (LILEs) are enriched, whereas the contents of Nb, Ta, P, Ti, Ba, Sr and high-field-strength elements (HFSEs) are depleted. The biotite and muscovite granites show no significant depletion in Zr and Hf.

4.b. Zircon U−Pb dating

The results of the zircon U−Pb dating of selected samples from the Hailesitai pluton are listed in Table 2. The morphologies and internal structures of the zircon grains in the biotite and muscovite granites suggest characteristics of an igneous nature. Under the polarizing microscope, these zircon grains showed no obvious evidence of complex internal structures (inclusions or inheritance), and most of them were sub-rounded to rounded in shape with well-defined oscillatory zoning in the cathodoluminescence images (Fig. 5). The zircon grains are 40−150 μm long and 40−80 μm wide with short columnar−granular or euhedral–subhedral shapes. The core−rim structures in the zircon grains are developed. Generally, the core of the individual grain is euhedral−subhedral or rounded−ovular in shape with solution structures, and the internal banded and oscillatory zones are developed. The zircon Pb (average 5.6), U (average 213.2) and Th (average ∼ 137.5) contents in both the biotite granite and muscovite granite are high and the Th/U ratios range from 0.4 to 1.1 (average ∼ 0.7). The concordant age of the earlier biotite granite (No. 4−2CN) is 161.2 ± 0.6 (mean square weighted deviation (MSWD) = 1.8, n = 27), and the analysis points are distributed on or beside the concordant line at the age of the concordant diagram (Fig. 6a). The concordant zircon age of the latter biotite granite (No. 4−1CN) is 151.9 ± 0.5 (MSWD = 0.95, n = 20) (Fig. 6b) and the concordant age of the muscovite granite (No. 9−1CN) is 152.1 ± 0.6 (MSWD = 1.8, n = 21) (Fig. 6c). The concordant ages of the latter granites are *c.* 152 Ma.

4.c. Hf isotope

The results from the zircon Hf isotope analysis of selected samples from the Hailesitai pluton are listed in Table 3. The $^{176}Yb/^{177}Hf$ and $^{176}Lu/^{177}Hf$ ratios of the 49 zircon grains are 0.015425−0.055594 and 0.000633−0.002214, respectively. The $^{176}Lu/^{177}Hf$ ratio is less than or close to 0.002, indicating that these zircons formed only with reduced levels of radiogenic Hf accumulation. The one-stage depleted mantle model

https://doi.org/10.1017/S0016756816000534 Published online by Cambridge University Press

Table 1. The whole rock analysis results of the Hailesitai pluton. Sample numbers are from 1H to 21H

Sample	1H	2H	3H	4H	5H	6H	7H	8H	9H	10H	11H	12H	13H	14H	15H	16H	17H	18H	19H	20H	21H
Lithology [a]	BG	BG	BG	MG	BG	BG	BG	BG	BG	BG	BG	BG	BG	BG	MG	TG	BG	MG	MG	MG	MG
Major elements (wt %)																					
SiO_2	75.14	77.23	75.11	76.56	77.05	75.19	77.19	75.93	74.53	77.18	76.93	75.25	76.58	75.84	76.04	76.14	75.31	76.22	75.72	76.02	75.92
TiO_2	0.19	0.10	0.20	0.21	0.09	0.22	0.14	0.16	0.29	0.17	0.17	0.17	0.18	0.09	0.18	0.21	0.23	0.16	0.18	0.15	0.18
Al_2O_3	13.74	12.18	13.56	12.46	12.55	12.93	12.23	13.74	13.33	12.12	12.30	13.52	12.14	13.24	13.00	12.37	12.79	12.98	12.42	12.66	12.86
Fe_2O_3	0.52	0.41	0.76	0.54	0.35	0.79	0.50	0.52	1.08	0.54	0.68	0.68	0.73	0.47	0.73	1.08	0.75	0.62	1.17	0.82	1.03
FeO	0.32	0.20	0.13	0.17	0.25	0.30	0.23	0.17	0.32	0.18	0.17	0.12	0.27	0.12	0.17	0.13	0.30	0.12	0.18	0.23	0.20
MnO	0.01	0.01	0.01	0.01	0.01	0.02	0.01	0.01	0.02	0.01	0.11	0.03	0.04	0.02	0.01	0.19	0.04	0.01	0.27	0.11	0.01
MgO	0.30	0.19	0.25	0.19	0.14	0.34	0.22	0.23	0.35	0.22	0.21	0.24	0.24	0.17	0.21	0.27	0.32	0.17	0.21	0.21	0.29
CaO	0.34	0.36	0.30	0.18	0.23	0.55	0.25	0.23	0.49	0.28	0.26	0.30	0.40	0.38	0.30	0.35	0.63	0.29	0.27	0.33	0.17
Na_2O	3.65	4.04	3.57	3.71	3.57	3.72	3.63	3.28	4.10	3.59	3.41	3.86	3.70	3.43	3.61	3.79	3.87	3.53	3.63	3.50	3.59
K_2O	4.95	4.49	5.33	5.00	5.11	5.04	4.82	5.00	4.65	4.76	4.89	4.95	4.83	5.57	4.93	4.74	4.63	5.02	4.98	5.24	4.66
P_2O_5	0.03	0.02	0.04	0.04	0.02	0.07	0.03	0.03	0.06	0.03	0.03	0.03	0.03	0.01	0.04	0.04	0.07	0.03	0.03	0.03	0.03
H_2O^+	0.51	0.43	0.45	0.68	0.46	0.67	0.60	0.54	0.63	0.60	0.70	0.62	0.54	0.51	0.62	0.54	0.87	0.70	0.78	0.56	0.93
CO_2	0.08	0.04	0.08	0.04	0.06	0.04	0.04	0.04	0.02	0.02	0.02	0.04	0.02	0.04	0.04	0.04	0.06	0.04	0.02	0.02	0.02
LOI	0.72	0.59	0.63	0.95	0.6	0.88	0.63	0.66	0.82	0.73	0.89	0.75	0.7	0.62	0.67	0.62	1.15	0.91	0.98	0.64	1.03
Total	100.5	100.3	100.4	100.7	100.5	100.8	100.5	100.5	100.7	100.4	100.8	100.6	100.4	100.5	100.6	100.5	101.0	100.8	100.8	100.5	100.9
ASI [b]	1.2	1.0	1.1	1.1	1.1	1.1	1.1	1.3	1.1	1.1	1.1	1.1	1.0	1.1	1.1	1.1	1.1	1.1	1.1	1.1	1.2
MALI [c]	8.3	8.2	8.6	8.5	8.5	8.2	8.2	8.1	8.3	8.1	8.0	8.5	8.1	8.6	8.2	8.2	7.9	8.3	8.3	8.4	8.1
lgC/KN [d]	–1.4	–1.4	–1.5	—1.7	–1.6	–1.2	–1.5	–1.6	–1.3	–1.5	–1.5	–1.5	–1.3	–1.4	–1.5	–1.4	–1.1	–1.5	–1.5	–1.4	–1.7
R1 [e]	2545	2662	2480	2614	2668	2496	2723	2721	2397	2756	2767	2481	2650	2531	2624	2600	2554	2649	2576	2583	2686
R2 [e]	323	289	313	276	280	332	280	308	334	281	282	312	295	311	300	296	338	297	286	296	288
Fe∗ [f]	0.72	0.69	0.77	0.70	0.83	0.73	0.71	0.91	0.73	0.79	0.75	0.83	0.71	0.82	0.74	0.80	0.84	0.78	0.91	0.86	0.85
FeO^{tot}/MgO	2.63	2.99	3.26	4.04	2.97	3.09	2.77	3.69	3.03	3.72	3.05	3.86	3.19	3.05	3.45	3.94	4.08	3.99	5.87	4.61	3.89
$Na_2O + K_2O$	8.60	8.53	8.90	8.71	8.68	8.76	8.45	8.28	8.75	8.35	8.30	8.81	8.53	9.00	8.54	8.53	8.50	8.55	8.61	8.74	8.25
K_2O/Na_2O	1.36	1.11	1.49	1.35	1.43	1.35	1.33	1.52	1.13	1.33	1.43	1.28	1.31	1.62	1.37	1.25	1.20	1.42	1.37	1.50	1.30
Trace elements (ppm)																					
Co	0.36	0.85	0.36	0.68	1.01	0.91	0.48	0.59	0.67	0.47	2.85	1.12	0.79	0.61	0.40	0.94	1.28	0.67	1.22	0.87	0.68
Cu	1.53	1.61	1.22	2.25	1.80	2.14	1.83	1.85	1.54	0.95	5.48	4.77	1.75	13.4	1.61	3.13	2.71	2.71	5.71	2.39	1.83
Zn	13.4	12.9	11.1	11.8	8.96	20.6	12.5	13.4	19.3	10.9	31.6	44.4	17.2	18.9	10.4	10.6	25.2	11.3	35.4	18.3	10.6
Zr	148	99.6	148	179	151	153	121	130	217	125	137	140	138	86.2	147	165	158	143	153	129	143
Pb	14.9	18.2	20.8	13.9	18.3	17.3	20.0	19.0	18.2	14.6	21.5	25.9	18.1	34.1	14.0	14.9	18.7	14.7	15.3	19.4	11.3
Hf	7.50	6.44	7.52	8.99	8.79	8.25	6.53	7.12	10.6	6.80	7.17	7.37	7.90	4.95	8.03	8.41	8.01	7.74	8.33	6.84	8.00
Ta	1.60	1.54	0.91	1.15	1.10	1.91	1.02	1.05	2.01	1.66	1.90	1.77	2.50	1.39	1.78	1.48	1.92	1.12	1.56	1.44	1.29
Cr	1.55	1.17	1.81	3.29	2.25	2.63	2.17	2.00	2.62	1.79	1.87	1.72	2.34	2.24	1.98	1.98	2.58	2.34	2.68	1.93	2.89
Ni	1.44	2.19	1.69	4.14	2.92	2.58	2.63	3.18	2.02	1.74	4.14	2.19	2.47	3.87	1.86	15.3	4.88	3.65	15.5	7.44	3.90
Sr	41.2	22.3	32.9	32.7	15.4	47.7	28.4	32.7	64.5	25.2	37.7	20.8	27.8	20.8	23.3	37.8	75.4	26.4	32.8	40.7	43.0
V	7.97	4.94	7.84	9.52	7.56	11.7	7.37	6.36	15.6	6.17	12.3	8.96	8.31	5.39	8.87	10.9	12.2	6.41	9.35	11.0	14.6
Th	50.58	37.83	42.38	58.71	39	28.86	27.99	40.26	42.28	33.6	49.86	54.32	42.69	40.12	27.47	39.74	42.27	48.31	40.04	46.96	43.42
U	2.954	10.34	8.483	7.389	12.15	3.978	6.334	5.608	3.9	5.143	11.48	11.2	7.526	5.029	7.752	6.27	8.204	8.681	8.935	4.201	3.599
Ba	91.93	48.61	95.85	101.1	35.7	209.3	112.1	111.8	168.7	59.8	165	88.5	76.8	43.7	78.4	174	245.2	75.96	211.9	118.1	115.4
Ga	22.13	24.56	20.89	23.32	23.03	23.16	22.68	22.55	24.21	23.63	22.01	21.67	23.69	20.99	23.61	22.99	23.18	22.35	22.69	24.52	24.38
Nb	16.6	18.1	10.42	12.18	12.95	18.87	12.06	13.07	23.51	19.13	22.4	20.55	26.02	13.96	21.27	18.81	24.15	15.62	18.2	16.4	13.87
Rb	335.7	345.8	347.3	348.6	370.1	339.2	324.1	342.4	310	338.6	344.7	326.9	310.8	224.5	325.2	323.7	287.5	319.9	322.2	335	337.1
Y	7.49	8.88	16.9	15.5	9.55	14.0	10.1	11.4	16.8	9.01	9.82	13.9	10.7	5.07	12.2	15.0	8.80	10.2	9.89	11.1	8.58
Ce	73.2	47.3	80.8	99.4	51.1	77.1	63.3	58.6	96.0	61.4	94.0	98.4	72.7	43.1	67.4	83.7	76.6	96.6	81.7	69.0	55.3
$10^4 \times Ga/Al$	3.04	3.81	2.91	3.54	3.47	3.38	3.50	3.10	3.43	3.68	3.38	3.03	3.69	3.00	3.43	3.51	3.42	3.25	3.45	3.66	3.58

Table 1. Continued.

Sample	1H	2H	3H	4H	5H	6H	7H	8H	9H	10H	11H	12H	13H	14H	15H	16H	17H	18H	19H	20H	21H
Lithology [a]	BG	BG	BG	MG	BG	BG	BG	BG	BG	BG	BG	BG	BG	BG	MG	TG	BG	MG	MG	MG	MG
Zr + Y + Nb + Ce	245.2	173.8	256.3	306.3	224.8	262.7	206.6	213.5	353.7	214.5	263.3	273.0	247.3	148.4	248.2	282.7	267.1	265.5	262.9	225.2	220.3
Nb + Ta	18.20	19.64	11.33	13.33	14.05	20.78	13.08	14.12	25.52	20.79	24.30	22.32	28.52	15.35	23.05	20.29	26.07	16.74	19.76	17.84	15.16
Nb/Ta	10.38	11.75	11.45	10.59	11.77	9.88	11.82	12.45	11.70	11.52	11.79	11.61	10.41	10.04	11.95	12.71	12.58	13.95	11.67	11.39	10.75
Zr/Hf	19.73	15.47	19.71	19.94	17.19	18.52	18.55	18.33	20.52	18.38	19.12	19.00	17.45	17.42	18.35	19.65	19.67	18.48	18.38	18.82	17.82
Th/U	17.12	3.66	5.00	7.95	3.21	7.26	4.42	7.18	10.84	6.53	4.34	4.85	5.67	7.98	3.54	6.34	5.15	5.57	4.48	11.18	12.07
Rb/Sr	8.15	15.47	10.57	10.66	23.98	7.12	11.40	10.47	4.81	13.42	9.13	15.74	11.17	10.78	13.94	8.56	3.82	12.13	9.83	8.23	7.84
Rb/Ba	3.65	7.11	3.62	3.45	10.37	1.62	2.89	3.06	1.84	5.66	2.09	3.69	4.05	5.14	4.15	1.86	1.17	4.21	1.52	2.84	2.92
Y/Nb	0.45	0.49	1.62	1.27	0.74	0.74	0.84	0.87	0.72	0.47	0.44	0.68	0.41	0.36	0.57	0.80	0.36	0.65	0.54	0.68	0.62
Ce/Nb	4.41	2.61	7.76	8.16	3.95	4.09	5.25	4.49	4.08	3.21	4.20	4.79	2.79	3.09	3.17	4.45	3.17	6.18	4.49	4.21	3.99
Rb/Nb	20.22	19.10	33.33	28.62	28.58	17.97	26.88	26.20	13.19	17.70	15.39	15.91	11.94	16.08	15.29	17.21	11.90	20.48	17.70	20.42	24.31
Nb/U	5.62	1.75	1.23	1.65	1.07	4.74	1.90	2.33	6.03	3.72	1.95	1.83	3.46	2.78	2.74	3.00	2.94	1.80	2.04	3.90	3.85
t_{Zr} [g]	833.2	790.9	831.6	847.6	832.2	829.8	811.1	825.4	865.0	813.8	824.0	825.9	820.1	781.1	831.1	838.2	832.4	828.6	831.6	815.9	830.1
Rare earth elements (ppm)																					
La	50.7	41.0	57.2	68.9	44.6	51.1	47.8	43.6	61.1	45.6	53.4	66.2	52.4	31.9	52.2	61.9	41.6	64.5	52.6	31.7	40.6
Ce	73.2	47.3	80.8	99.4	51.1	77.1	63.3	58.6	96.0	61.4	94.0	98.4	72.7	43.1	67.4	83.7	76.6	96.6	81.7	69.0	55.3
Pr	6.29	3.10	6.93	8.40	3.29	7.09	5.06	4.63	8.85	4.70	5.84	7.03	6.12	2.96	5.73	7.65	5.03	7.29	5.74	3.87	4.75
Nd	17.1	7.03	19.3	23.3	7.04	20.7	13.6	12.1	27.0	12.4	15.4	18.4	16.8	7.08	15.4	21.2	13.6	19.0	15.1	10.7	12.9
Sm	2.54	1.05	3.08	3.53	1.04	3.42	2.13	1.94	4.57	1.89	2.27	2.72	2.63	0.980	2.34	3.40	2.04	2.89	2.30	1.90	1.87
Eu	0.36	0.17	0.39	0.37	0.16	0.48	0.33	0.29	0.50	0.24	0.30	0.35	0.33	0.19	0.29	0.45	0.38	0.34	0.31	0.32	0.30
Gd	1.85	1.07	2.45	2.78	1.12	2.74	1.79	1.78	3.51	1.67	1.99	2.45	1.93	0.853	2.01	2.75	1.80	2.20	1.98	1.82	1.44
Tb	0.24	0.16	0.39	0.42	0.17	0.38	0.26	0.29	0.54	0.24	0.27	0.35	0.29	0.13	0.30	0.43	0.26	0.30	0.28	0.29	0.21
Dy	1.19	0.976	2.22	2.24	1.12	2.07	1.49	1.67	2.83	1.40	1.51	1.93	1.57	0.756	1.71	2.42	1.48	1.56	1.53	1.78	1.32
Ho	0.24	0.20	0.49	0.47	0.25	0.40	0.32	0.37	0.55	0.29	0.32	0.42	0.33	0.16	0.36	0.49	0.31	0.32	0.33	0.37	0.29
Er	0.79	0.76	1.63	1.52	0.94	1.27	1.06	1.22	1.70	1.00	1.10	1.40	1.14	0.54	1.26	1.58	1.01	1.10	1.14	1.14	1.03
Tm	0.14	0.14	0.28	0.25	0.20	0.20	0.18	0.21	0.26	0.17	0.19	0.23	0.20	0.12	0.22	0.26	0.17	0.18	0.20	0.20	0.17
Yb	1.23	1.30	2.34	2.14	2.03	1.63	1.56	1.85	2.20	1.54	1.67	2.19	1.85	0.96	1.95	2.18	1.45	1.68	1.77	1.65	1.51
Lu	0.22	0.25	0.42	0.38	0.40	0.29	0.28	0.33	0.38	0.28	0.31	0.39	0.34	0.18	0.35	0.38	0.26	0.31	0.32	0.28	0.26
Y	7.49	8.88	16.87	15.48	9.55	13.98	10.12	11.37	16.83	9.01	9.82	13.90	10.66	5.07	12.19	15.01	8.80	10.23	9.89	11.08	8.58
Total	164	113	195	230	123	183	149	140	227	142	188	216	169	94.9	164	204	155	208	175	136	131
ΣREE	156.1	104.4	177.9	214.1	113.5	168.9	139.2	129.0	210.0	132.8	178.6	202.5	158.6	89.9	151.5	188.8	146.1	198.2	165.3	125.0	121.9
Nb/La	0.3	0.4	0.2	0.2	0.3	0.4	0.3	0.3	0.4	0.4	0.4	0.3	0.5	0.4	0.4	0.3	0.6	0.2	0.3	0.5	0.3
LREE	150.2	99.6	167.7	203.9	107.3	159.9	132.2	121.2	198.1	126.3	171.2	193.1	151.0	86.2	143.4	178.3	139.3	190.6	157.7	117.4	115.7
HREE	5.9	4.9	10.2	10.2	6.2	9.0	6.9	7.7	12.0	6.6	7.4	9.4	7.6	3.7	8.1	10.5	6.7	7.7	7.6	7.5	6.2
LREE/HREE	25.5	20.4	16.4	20.0	17.2	17.8	19.1	15.7	16.6	19.2	23.2	20.6	19.8	23.3	17.6	17.0	20.6	24.9	20.9	15.6	18.6
La_N/Yb_N	29.5	22.6	17.5	23.1	15.8	22.5	22.0	16.9	19.9	21.3	22.9	21.7	20.3	23.9	19.2	20.3	20.5	27.5	21.3	13.8	19.3
δEu [h]	0.5	0.5	0.4	0.4	0.5	0.5	0.5	0.5	0.4	0.4	0.4	0.4	0.4	0.6	0.4	0.5	0.6	0.4	0.4	0.5	0.6
δCe [h]	1.0	1.0	1.0	1.0	1.0	1.0	1.0	1.0	1.0	1.0	1.3	1.1	1.0	1.1	1.0	0.9	1.3	1.1	1.2	1.5	1.0

[a]Lithology: HG, biotite granite; MG, muscovite granite; TG, two-mica granite.
[b]Aluminium Saturation Index, ASI = Al/(Ca− 1.67P + Na + K), molecular ratio.
[c]Modified Alkali-Lime Index, MALI = $Na_2O + K_2O - CaO$, wt %.
[d]lgC/NK = lg CaO/($Na_2O + K_2O$), wt %.
[e]R1 = 4Si − 11(Na + K) − 2(Fe + Ti), R2 = 6Ca + 2Mg + Al, molecular ratio.
[f]Fe∗ = FeO^{tot}/(FeO^{tot} + MgO), FeO^{tot} = FeO + 0.8998∗Fe_2O_3, wt %.
[g]t_{Zr} /°C = 12 900/[2.95 + 0.85M + ln(496 000/Zr_{melt})] − 273.15, M = (Na + K + 2Ca) /(Al × Si), mole ratio; Zr_{melt} is the Zr content in the magma (Miller, Meschterwell & Mapes, 2003).
[h]$\delta Eu = Eu_N/(Sm_N \times Gd_N)^{1/2}$, $\delta Ce = Ce_N/(La_N \times Pr_N)^{1/2}$, where *N* denotes chondrite normalization. The chondrite values are from McDonough & Sun (1995).

Table 2. Zircon U–Pb dating analysis results of the Hailesitai pluton. Sample numbers are 4-1CN, 4-2CN and 9-1CN.

	Contents ($\times 10^{-6}$)				Isotope ratio						Age(Ma)					
Sample No.	Pb	Th	U	Th/U	$^{207}Pb/^{206}Pb$	1σ	$^{207}Pb/^{235}U$	1σ	$^{206}Pb/^{238}U$	1σ	$^{207}Pb/^{206}Pb$	1σ	$^{207}Pb/^{235}U$	1σ	$^{206}Pb/^{238}U$	1σ
4–1CN (biotite granite)																
1	4.5	127.6	165.8	0.8	0.04935	0.0036	0.16253	0.0121	0.02388	0.00017	165	169	153	11	152	1
2	3.7	102.3	139.1	0.7	0.04811	0.0033	0.15963	0.0110	0.02406	0.00019	105	161	150	10	153	1
3	3.3	101.3	129.6	0.8	0.04885	0.0054	0.15950	0.0178	0.02368	0.00022	141	258	150	17	151	1
4	4.8	148.7	178.0	0.8	0.04790	0.0030	0.15836	0.0100	0.02398	0.00015	94	149	149	9	153	1
5	7.4	183.3	299.2	0.6	0.04720	0.0021	0.15610	0.0074	0.02398	0.00015	60	106	147	7	153	1
6	10.3	216.1	421.8	0.5	0.04799	0.0023	0.15756	0.0077	0.02381	0.00015	99	112	149	7	152	1
7	2.5	85.1	95.8	0.9	0.04827	0.0078	0.15845	0.0254	0.02381	0.00031	112	380	149	24	152	2
8	11.4	293.3	468.8	0.6	0.04889	0.0011	0.15956	0.0034	0.02367	0.00014	142	51	150	3	151	1
9	19.8	567.4	791.1	0.7	0.04828	0.0009	0.15901	0.0031	0.02389	0.00013	113	45	150	3	152	1
10	4.5	147.7	171.6	0.9	0.04961	0.0028	0.16136	0.0092	0.02359	0.00014	177	133	152	9	150	1
11	3.8	158.2	139.8	1.1	0.04953	0.0047	0.16233	0.0156	0.02377	0.00024	173	224	153	15	151	2
12	7.4	187.0	288.4	0.6	0.04993	0.0016	0.16430	0.0052	0.02387	0.00013	192	72	154	5	152	1
13	3.3	93.5	126.2	0.7	0.04894	0.0039	0.16246	0.0130	0.02408	0.00018	145	189	153	12	153	1
14	7.2	197.8	270.6	0.7	0.04841	0.0016	0.16100	0.0056	0.02412	0.00015	119	80	152	5	154	1
15	8.2	300.1	295.6	1.0	0.04817	0.0014	0.15870	0.0046	0.02389	0.00014	108	66	150	4	152	1
16	3.8	100.4	159.8	0.6	0.04886	0.0027	0.15988	0.0089	0.02373	0.00017	141	127	151	8	151	1
17	5.1	133.8	194.1	0.7	0.04833	0.0022	0.15816	0.0074	0.02373	0.00015	116	110	149	7	151	1
18	4.1	94.6	165.0	0.6	0.04965	0.0021	0.16255	0.0068	0.02374	0.00015	179	97	153	6	151	1
19	3.0	80.9	114.8	0.7	0.04839	0.0025	0.15721	0.0083	0.02356	0.00016	119	124	148	8	150	1
20	2.4	55.5	87.8	0.6	0.04949	0.0047	0.16349	0.0153	0.02396	0.00018	171	223	154	14	153	1
4–2CN (biotite granite)																
1	5.9	118.0	211.5	0.6	0.050313	0.0015	0.17455	0.0053	0.025162	0.00014	210	70	163	5	160	1
2	5.1	123.3	179.2	0.7	0.048075	0.0018	0.16862	0.0064	0.025438	0.00015	103	88	158	6	162	1
3	5.7	105.7	218.7	0.5	0.048386	0.0016	0.16687	0.0055	0.025013	0.00014	118	78	157	5	159	1
4	3.4	56.9	130.6	0.4	0.049303	0.0025	0.17125	0.0088	0.025192	0.00015	162	119	161	8	160	1
5	6.6	140.2	245.3	0.6	0.048213	0.0017	0.16898	0.0059	0.025419	0.00016	110	83	159	6	162	1
6	4.9	88.1	186.9	0.5	0.048392	0.0020	0.16895	0.0071	0.025322	0.00016	118	97	159	7	161	1
7	4.6	103.1	165.4	0.6	0.049356	0.0029	0.17343	0.0102	0.025485	0.00020	165	136	162	10	162	1
8	3.8	92.6	140.8	0.7	0.049132	0.0019	0.17101	0.0068	0.025243	0.00016	154	92	160	6	161	1
9	5.8	147.5	208.4	0.7	0.049438	0.0018	0.17261	0.0064	0.025323	0.00015	169	87	162	6	161	1
10	6.9	187.5	254.3	0.7	0.048892	0.0013	0.16755	0.0045	0.024855	0.00015	143	63	157	4	158	1
11	3.5	81.8	132.7	0.6	0.049189	0.0017	0.16987	0.0059	0.025046	0.00018	157	79	159	6	159	1
12	4.8	92.2	178.1	0.5	0.049647	0.0020	0.17452	0.0070	0.025495	0.00016	178	92	163	7	162	1

Table 2. Continued.

Sample No.	Contents ($\times 10^{-6}$)			Th/U	Isotope ratio						Age(Ma)					
	Pb	Th	U		$^{207}Pb/^{206}Pb$	1σ	$^{207}Pb/^{235}U$	1σ	$^{206}Pb/^{238}U$	1σ	$^{207}Pb/^{206}Pb$	1σ	$^{207}Pb/^{235}U$	1σ	$^{206}Pb/^{238}U$	1σ
13	6.0	140.3	218.7	0.6	0.048992	0.0016	0.17220	0.0055	0.025492	0.00015	147	74	161	5	162	1
14	3.8	91.6	141.9	0.6	0.048393	0.0020	0.16869	0.0072	0.025281	0.00016	119	100	158	7	161	1
15	4.3	85.6	162.8	0.5	0.049964	0.0024	0.17391	0.0083	0.025245	0.00016	193	112	163	8	161	1
16	5.8	138.3	208.2	0.7	0.049621	0.0032	0.17468	0.0109	0.025531	0.00021	177	149	163	10	163	1
17	2.5	51.7	90.9	0.6	0.048283	0.0044	0.16906	0.0153	0.025395	0.00020	113	215	159	14	162	1
18	9.1	321.6	305.7	1.1	0.048457	0.0011	0.16881	0.0040	0.025266	0.00015	122	53	158	4	161	1
19	10.4	187.7	392.9	0.5	0.049705	0.0009	0.17465	0.0032	0.025485	0.00014	181	42	163	3	162	1
20	1.9	50.9	65.4	0.8	0.049956	0.0044	0.17409	0.0151	0.025274	0.00022	193	204	163	14	161	1
21	5.8	91.3	220.6	0.4	0.049203	0.0016	0.17228	0.0058	0.025395	0.00015	158	78	161	5	162	1
22	6.1	105.3	235.9	0.4	0.050713	0.0014	0.17471	0.0050	0.024986	0.00015	228	65	163	5	159	1
23	0.9	25.9	31.1	0.8	0.048470	0.0137	0.16908	0.0428	0.025300	0.00044	122	667	159	40	161	3
24	4.2	120.0	148.5	0.8	0.049551	0.0023	0.17297	0.0079	0.025317	0.00015	174	106	162	7	161	1
25	3.3	79.9	127.7	0.6	0.048706	0.0024	0.17374	0.0087	0.025871	0.00017	134	117	163	8	165	1
26	2.3	48.1	84.4	0.6	0.049146	0.0035	0.17353	0.0126	0.025608	0.00020	155	169	162	12	163	1
27	3.3	89.2	116.1	0.8	0.047998	0.0030	0.16939	0.0107	0.025595	0.00017	99	149	159	10	163	1
9−1CN (muscovite granite)																
1	3.4	78.3	129.9	0.6	0.0487	0.0042	0.1602	0.0139	0.0238	0.00019	136	202	151	13	152	1
2	7.8	123.2	317.6	0.4	0.0493	0.0022	0.1623	0.0072	0.0239	0.00014	164	103	153	7	152	1
3	6.8	137.8	258.6	0.5	0.0486	0.0020	0.1627	0.0068	0.0243	0.00014	128	96	153	6	155	1
4	3.2	87.0	123.7	0.7	0.0484	0.0025	0.1584	0.0083	0.0237	0.00016	120	121	149	8	151	1
5	6.4	146.2	246.2	0.6	0.0477	0.0044	0.1564	0.0143	0.0238	0.00019	86	218	148	13	151	1
6	24.2	473.9	793.9	0.6	0.0898	0.0029	0.3336	0.0096	0.0269	0.00016	1422	61	292	8	171	1
7	7.3	195.3	273.6	0.7	0.0487	0.0016	0.1606	0.0057	0.0239	0.00014	134	80	151	5	152	1
8	10.8	188.0	441.4	0.4	0.0482	0.0011	0.1585	0.0038	0.0238	0.00013	110	55	149	4	152	1
9	3.4	76.3	136.3	0.6	0.0492	0.0019	0.1610	0.0062	0.0237	0.00015	156	90	152	6	151	1
10	6.1	153.9	239.1	0.6	0.0487	0.0016	0.1597	0.0054	0.0238	0.00014	133	79	150	5	152	1
11	3.3	126.7	125.5	1.0	0.0496	0.0035	0.1612	0.0114	0.0236	0.00016	178	165	152	11	150	1
12	2.1	78.2	77.6	1.0	0.0493	0.0038	0.1615	0.0124	0.0238	0.00019	160	179	152	12	151	1
13	5.0	135.1	192.1	0.7	0.0494	0.0022	0.1628	0.0075	0.0239	0.00014	165	106	153	7	152	1
14	4.2	78.1	172.2	0.5	0.0489	0.0017	0.1624	0.0059	0.0241	0.00015	142	84	153	6	153	1
15	6.9	197.3	266.3	0.7	0.0494	0.0016	0.1612	0.0054	0.0237	0.00013	166	78	152	5	151	1
16	3.6	121.6	138.3	0.9	0.0489	0.0039	0.1605	0.0132	0.0238	0.00020	145	188	151	12	152	1
17	4.0	102.0	165.6	0.6	0.0477	0.0020	0.1575	0.0069	0.0239	0.00017	85	101	148	6	152	1
18	11.4	229.4	446.2	0.5	0.0466	0.0016	0.1568	0.0054	0.0244	0.00013	29	81	148	5	155	1
19	4.4	107.2	171.6	0.6	0.0493	0.0022	0.1617	0.0076	0.0238	0.00015	164	106	152	7	151	1
20	6.0	154.9	234.6	0.7	0.0498	0.0015	0.1636	0.0050	0.0238	0.00013	188	71	154	5	152	1
21	3.3	89.0	123.5	0.7	0.0495	0.0050	0.1625	0.0165	0.0238	0.00019	174	236	153	15	152	1
22	3.2	70.9	128.0	0.6	0.0478	0.0029	0.1573	0.0097	0.0239	0.00017	87	145	148	9	152	1

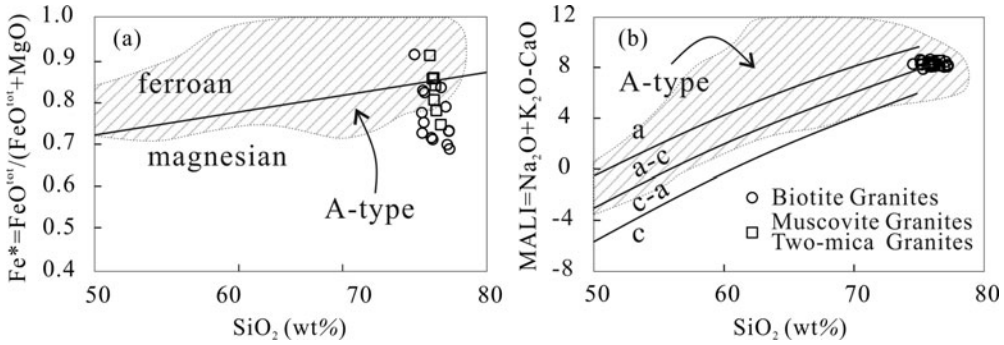

Figure 3. Geochemistry characteristic diagrams of Hailesitai pluton. (a) SiO_2 versus Fe^* and (b) SiO_2 versus MALI are from Frost *et al.* (2001), $Fe^* = FeO^{tot}/(FeO^{tot} + MgO)$, $FeO^{tot} = FeO + 0.8998 * Fe_2O_3$ (wt %); Modified Alkali-Lime Index, $MALI = Na_2O + K_2O + CaO$ (wt %); c, calcic, a, alkali.

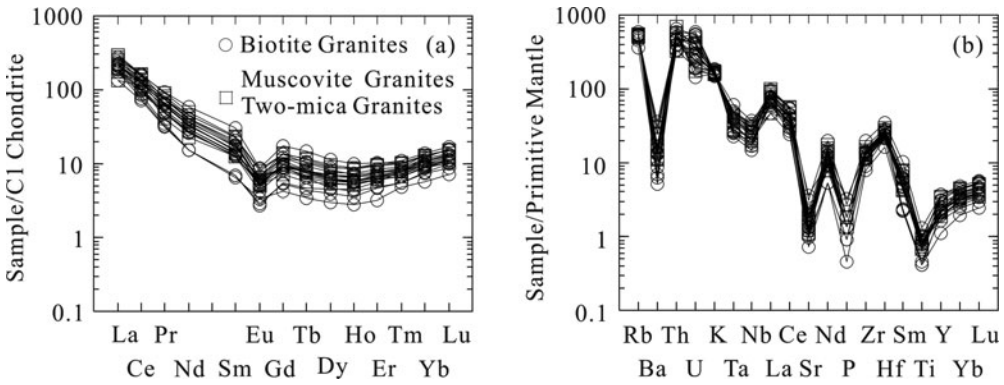

Figure 4. REE and trace elements distribution curves of Hailesitai pluton. Normalized spherical meteorite data is from Pearce, Harris & Tindle (1984), and normalized primordial mantle data is after McDonough & Sun (1995).

of the 49 zircons provides dates of 450–586 Ma, and the two-stage depleted mantle model provides dates of 569–738 Ma. In addition, the $\varepsilon_{Hf}(t)$ values, except for the value of No. 4−1CN−02 (+2.82), fluctuate around the average value of +4.51 with a range of 3.64–5.70. The $^{176}Hf/^{177}Hf$ ratios of the three samples (Nos. 4−1CN, 9−1CN, 4−2CN) range from 0.282852 to 0.282933. The Hf composition characteristics of the inherited zircon (Spot No. 9−1CN−6) is similar to the granite of the Hailesitai pluton. Therefore, these zircon granite samples have relatively homogeneous Hf isotope compositions (Fig. 7).

5. Discussion

5.a. Genesis

Hailesitai granites exhibit the geochemical characteristics of peraluminous and high-K calc-alkaline (Table 1), which are similar to A-type granites (Eby, 1990, 1992). With respect to I- and S-type granites, A-type granites show geochemical characteristics of high $Na_2O + K_2O$, Fe^*, Ga/Al and HFSE values, and low Sr, Ti, Ba and Eu values (Table 1; Fig. 4). The high Zr content (average 143 ppm) and the high zircon saturation temperatures (Table 1) (781.1−865.0 °C, average 825.7 °C) show a higher isothermal surface of formation, which indicates the A-type characteristics.

Eby (1990) suggests that A-type granites can be divided into two chemical groups and successfully discriminated by utilizing incompatible elements Rb, Ce, Y, Nb, Zr, Hf, Th and Ga. In the 10000∗Ga/Al and $Na_2O + K_2O$ diagram (Fig. 8), samples fall into the A-type granites field, and in the Nb−Y−Ce and Nb−Y−Ga diagram (Fig. 9) most of the samples intensively distribute in the A1-type granites field.

These A1-type granites are significantly enriched in K, Rb and REEs with strong Eu, Ba, P, Ti and Sr negative anomalies (Fig. 4).The characteristics of low Ba and Sr indicate a source region of relatively shallow depth, possibly within the plagioclase or hornblende stability field in the lower crust (Ge *et al.* 2000; Ma *et al.* 2004). During the partial melting of plagioclase and hornblende, their residual phases reside in the source region, resulting in both the depletion of Ba, Sr and Eu and the heavy REEs (Ma *et al.* 2004; C. Zhang *et al.* 2014), which coincide with the presence of alkali feldspar and quartz as the characteristic principal phenocryst minerals. In terms of peraluminous (ASI, average 1.1, Table 1) and calc-alkaline (Fig. 3), Hailesitai granites are similar to the peraluminous granitoids that may be formed by partial melts of granitic crust at low pressure (Frost & Frost, 2010).

Therefore, the geochemical characteristics indicate that the Hailesitai granites belong to A-type granites defined as alkaline, anhydrous and anorogenic (Loiselle

https://doi.org/10.1017/S0016756816000534 Published online by Cambridge University Press

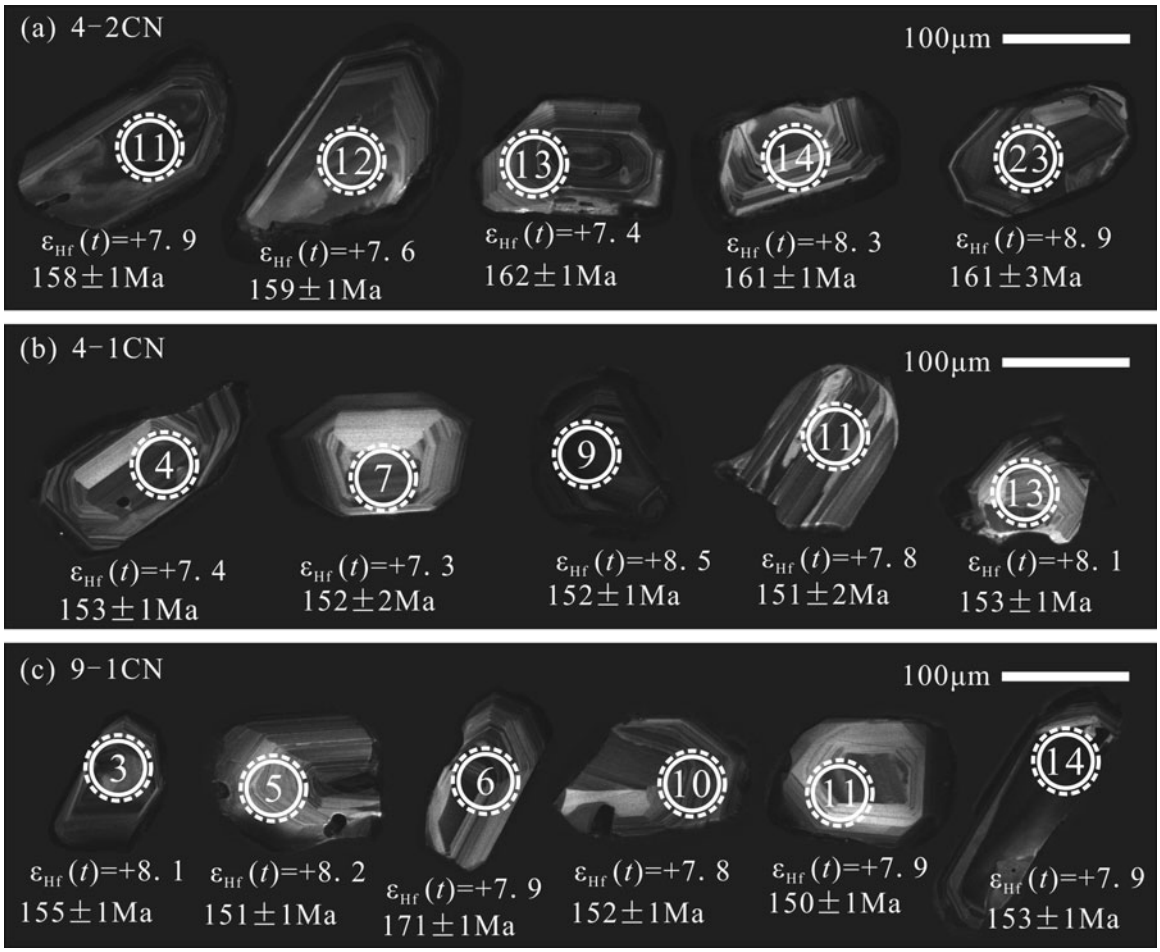

Figure 5. Zircon cathodoluminescence photographs of Hailesitai pluton: (a) 4-2CN, (b) 4-1CN and (c) 9-1CN. Representative CL images of zircon. Solid circle is the position for U–Pb isotope analysis, and dotted circle is for Hf isotope analysis.

& Wones, 1979) and emplaced into a non-orogenic setting within plate and along plate tectnic (Eby, 1990).

5.b. Substance origin

Three sets of chronological data used in this study indicate that the Hailesitai granites were erupted during the Late Jurassic. This is consistent with the findings of former studies of Mesozoic intrusive rocks in the GKR, which were mainly erupted during the middle Jurassic to early Cretaceous (Wang & Zhao, 1997; Wang *et al.* 2012; Cui *et al.* 2013; Sun *et al.* 2013, 2014; Zhu *et al.* 2013; X. Zhang *et al.* 2015). The geochemical characteristics of the samples could represent the source region and reflect the genesis of the plutons (L. Zhang *et al.* 2008; Zhang, Zuo & Cheng, 2014). The biotite and muscovite granites exhibit similar geochemical and chronological characteristics, which suggests they are products of the same geological environment and origin. The Hailesitai pluton has significantly lower Nb/Ta (average 11.53, Table 1) and HFSE values than the chondrite and primitive mantle (Table 1) (McDonough & Sun, 1995). This might be due to the crystallization of rutile, ilmenite and titanomagnetite (Barth, Nough & Rudnick, 2000). The lower Nb/U values (1.07−6.03; average 2.83) of the Hailesitai samples compared with the MORB and OIB (average 47 ± 10) also suggest the appearance of crustal contamination (Hofmann, 1986). Therefore, the melting originating from dehydrated oceanic crust might have acted on the magma sourced from the mantle. Eby (1990, 1992) has discussed the origin of the A1-type granites and has argued that they are the fractional crystallization product of mantle-derived magmas with/without interaction with crustal rocks (Foland & Allen, 1991; Kerr & Fryer, 1993). Furthermore, the Hf isotopic compositions of the Hailesitai samples (Fig. 8) also show that the Hailesitai pluton likely originated from a mixture of juvenile and crustal source rocks. Zhou *et al.* (2009) suggested that the mantle end-member components in the GKR were inherited from enriched lithospheric mantle beneath old blocks with overprint of subducted juvenile island arc materials. The Sr−Nd−Pb isotope ratios of late Mesozoic volcanic rocks in the GKR are similar to an enriched (EM1-type) mantle component originated by an ancient metasomatic event (Zhou *et al.* 2009; Huang *et al.* 2014). Thus, the Hailesitai pluton might be sourced from enriched (EM1-type) mantle that was a mixture of juvenile and crustal source rocks.

https://doi.org/10.1017/S0016756816000534 Published online by Cambridge University Press

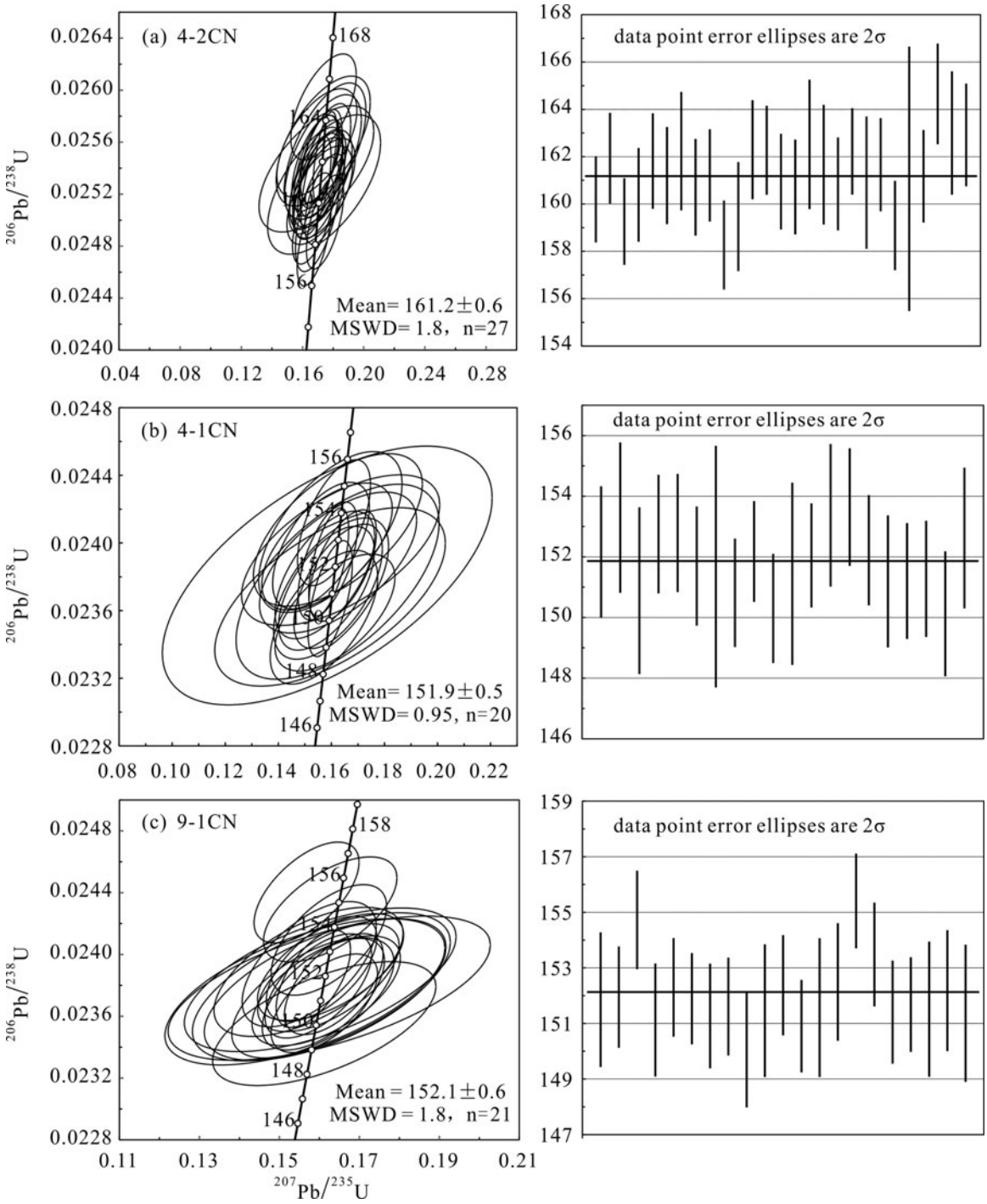

Figure 6. Concordia diagrams of zircon U–Pb dating of Hailesitai pluton: (a) 4-2CN, (b) 4-1CN and (c) 9-1CN. The unit of mean numbers are Ma.

5.c. Tectonic setting and geodynamic model

The A1-type granites represent differentiates of magmas derived from sources like those of oceanic-island basalts but emplaced in continental rifts or during intraplate magmatism (Eby, 1992). In the R1 and R2 diagram (Fig. 10), Hailesitai granites show the anorogenic tectonic setting. The coarse crystalline particles in the Hailesitai granitic pluton indicated slow uplift of the magma chamber (Zhang, Sun & Mao, 2006). This was related to the underplating of the mantle-derived magma, which might have resulted in a closed magma chamber under extensional conditions (Wang *et al*. 2015).

Several schemes interpreting the Mesozoic extensional tectonic setting of the GKR have been proposed. A mantle plume has been considered responsible for the formation of such large volumes of granite (Ge *et al.* 1999; Lin *et al.* 2003; Shao *et al.* 2010). However, the linear distribution of the Mesozoic granitic rocks along the GKR, even extending into eastern China, does not support this interpretation. Moreover, magmatic activities within the GKR extended from 185 to 105 Ma (Wang *et al.* 2006; Wu *et al.* 2011), which is

https://doi.org/10.1017/S0016756816000534 Published online by Cambridge University Press

Table 3. Hf isotope analysis (4-1CN, 4-2CN, 9-1CN) results of the Hailesitai pluton. Sample numbers are 4-1CN, 4-2CN and 9-1CN.

Sample No.	T (Ma)	$^{176}Yb/^{177}Hf$	$^{176}Lu/^{177}Hf$	$^{176}Hf/^{177}Hf$	2σ	$\varepsilon_{Hf}(0)$	$\varepsilon_{Hf}(t)$	T_{DM1}	T_{DM2}	$f_{Lu/Hf}$
4–1CN (biotite granite)										
4−1CN−01	152	0.026742	0.001091	0.282896	0.000018	4.4	7.6	506	645	−0.97
4−1CN−02	153	0.055594	0.002197	0.282852	0.000023	2.8	6.0	586	738	−0.93
4−1CN−03	151	0.019154	0.000809	0.282900	0.000021	4.5	7.8	496	635	−0.98
4−1CN−04	153	0.017842	0.000808	0.282888	0.000017	4.1	7.4	514	659	−0.98
4−1CN−05	153	0.033907	0.001356	0.282891	0.000019	4.2	7.4	516	655	−0.96
4−1CN−06	152	0.041434	0.001642	0.282876	0.000021	3.7	6.9	542	687	−0.95
4−1CN−07	152	0.016452	0.000746	0.282887	0.000016	4.1	7.3	514	660	−0.98
4−1CN−08	151	0.019775	0.000973	0.282895	0.000018	4.3	7.6	506	647	−0.97
4−1CN−09	152	0.045831	0.002214	0.282923	0.000018	5.3	8.5	482	597	−0.93
4−1CN−10	150	0.034175	0.001348	0.282926	0.000024	5.4	8.6	466	587	−0.96
4−1CN−11	151	0.018510	0.000788	0.282901	0.000023	4.6	7.8	495	633	−0.98
4−1CN−12	152	0.031535	0.001258	0.282891	0.000020	4.2	7.4	515	654	−0.96
4−1CN−13	153	0.032516	0.001295	0.282908	0.000018	4.8	8.1	491	621	−0.96
4−1CN−14	154	0.015425	0.000633	0.282894	0.000019	4.3	7.6	502	645	−0.98
4−1CN−15	152	0.034102	0.001361	0.282885	0.000018	4.0	7.2	525	668	−0.96
4−1CN−16	151	0.025354	0.001028	0.282890	0.000017	4.2	7.4	514	657	−0.97
4–2CN (biotite granite)										
4−2CN−11	158	0.028671	0.001138	0.282901	0.000020	4.5	7.9	500	633	−0.97
4−2CN−12	159	0.021579	0.000881	0.282891	0.000020	4.2	7.6	511	651	−0.97
4−2CN−13	162	0.032276	0.001503	0.282885	0.000018	4.0	7.4	527	665	−0.95
4−2CN−14	162	0.032622	0.001262	0.282909	0.000019	4.9	8.3	489	615	−0.96
4−2CN−15	161	0.025209	0.001024	0.282904	0.000018	4.7	8.1	494	625	−0.97
4−2CN−16	161	0.027741	0.001152	0.282921	0.000017	5.3	8.7	472	593	−0.97
4−2CN−17	163	0.026942	0.001107	0.282912	0.000021	5.0	8.4	483	608	−0.97
4−2CN−18	162	0.020282	0.000842	0.282922	0.000022	5.3	8.8	466	588	−0.97
4−2CN−19	161	0.048900	0.001932	0.282912	0.000021	4.9	8.3	495	615	−0.94
4−2CN−20	162	0.018569	0.000792	0.282909	0.000020	4.8	8.3	484	613	−0.98
4−2CN−21	161	0.019012	0.000789	0.282913	0.000023	5.0	8.5	477	605	−0.98
4−2CN−22	162	0.027209	0.001042	0.282877	0.000019	3.7	7.2	531	677	−0.97
4−2CN−23	159	0.026328	0.001088	0.282928	0.000018	5.5	8.9	461	579	−0.97
4−2CN−24	161	0.022037	0.000897	0.282902	0.000019	4.6	8.0	495	628	−0.97
4−2CN−25	161	0.027073	0.001082	0.282902	0.000017	4.6	8.0	497	629	−0.97
4−2CN−26	165	0.027889	0.001108	0.282890	0.000018	4.2	7.7	515	652	−0.97
4−2CN−27	163	0.017608	0.000740	0.282900	0.000019	4.5	8.0	495	629	−0.98
4−2CN−28	163	0.029658	0.001188	0.282877	0.000019	3.7	7.2	535	679	−0.96
9–1CN (muscovite granite)										
9−1CN−01	152	0.029795	0.001204	0.282875	0.000023	3.6	6.9	538	687	−0.96
9−1CN−02	152	0.017966	0.000725	0.282894	0.000018	4.3	7.6	503	646	−0.98
9−1CN−03	155	0.020701	0.000851	0.282907	0.000020	4.8	8.1	487	620	−0.97
9−1CN−04	151	0.018912	0.000811	0.282892	0.000018	4.3	7.5	507	651	−0.98
9−1CN−05	151	0.021540	0.000881	0.282913	0.000021	5.0	8.2	480	611	−0.97
9−1CN−06	171	0.018615	0.000761	0.282891	0.000020	4.2	7.9	508	644	−0.98
9−1CN−07	152	0.026639	0.001098	0.282908	0.000022	4.8	8.0	490	622	−0.97
9−1CN−08	152	0.019500	0.000819	0.282933	0.000024	5.7	9.0	450	569	−0.98
9−1CN−09	151	0.023323	0.001048	0.282912	0.000028	5.0	8.2	482	612	−0.97
9−1CN−10	152	0.018094	0.000745	0.282901	0.000018	4.6	7.8	495	633	−0.98
9−1CN−11	150	0.026333	0.001055	0.282894	0.000018	4.3	7.5	508	648	−0.97
9−1CN−12	151	0.015977	0.000674	0.282895	0.000018	4.3	7.6	502	645	−0.98
9−1CN−13	152	0.029309	0.001205	0.282916	0.000018	5.1	8.3	479	606	−0.96
9−1CN−14	153	0.031444	0.001307	0.282895	0.000019	4.3	7.6	511	648	−0.96
9−1CN−15	151	0.028254	0.001125	0.282896	0.000019	4.4	7.6	506	644	−0.97

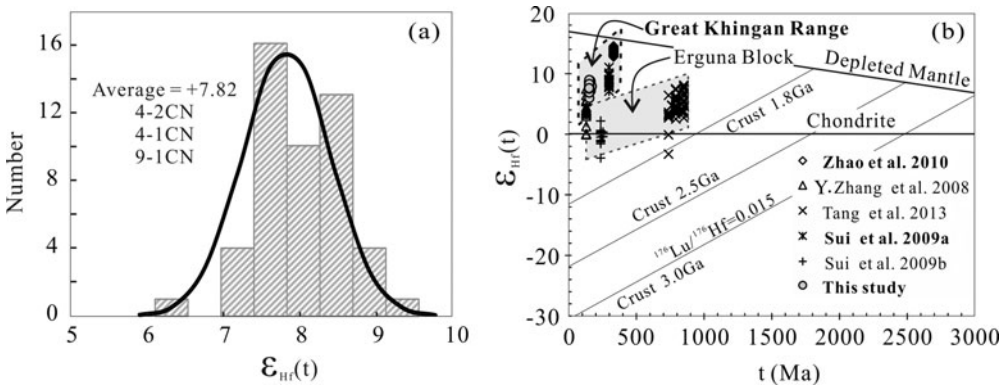

Figure 7. (a) Histogram of initial Hf isotope ratio. (b) Compilation diagram of $\varepsilon_{Hf}(t)$ versus U–Pb ages. The samples are 4-2CN, 4-1CN and 9-1CN. Data cited from Zhang, Ge & Liu (2008), Sui *et al.* (2009*a*, *b*), Zhao *et al.* (2010) and Tang *et al.* (2013).

https://doi.org/10.1017/S0016756816000534 Published online by Cambridge University Press

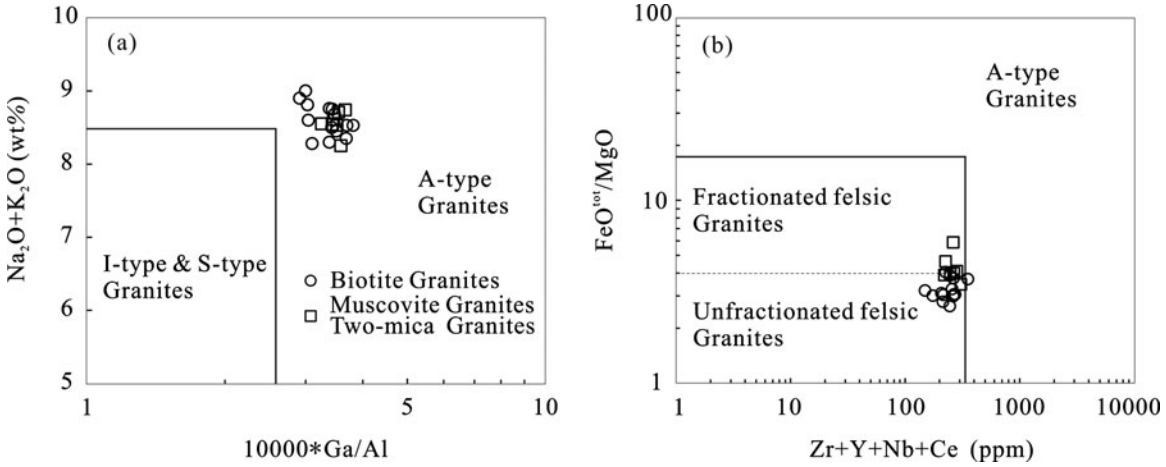

Figure 8. Diagram of discriminate genesis of Hailesitai granites. The original plot is after Whale (1987). (a) 10000*Ga versus Na_2O+K_2O diagram; (b) Zr+Y+Nb+Ce versus FeO^{tot}/MgO diagram.

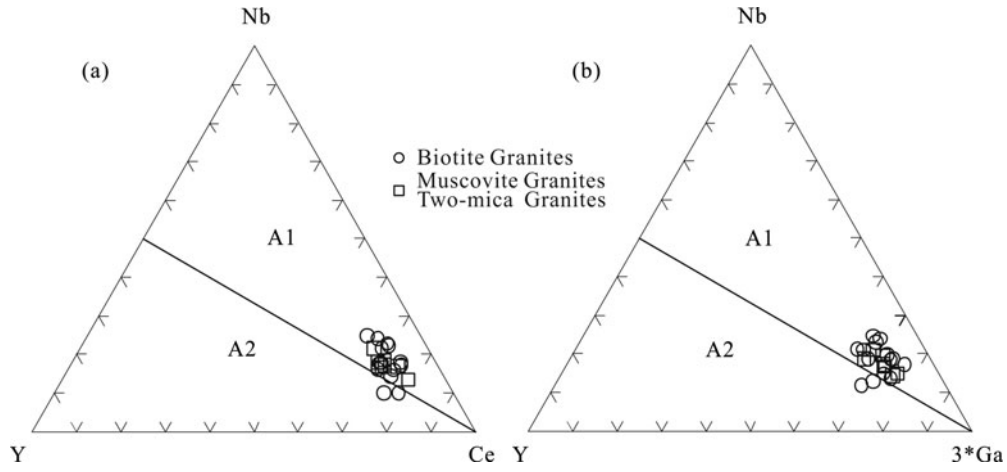

Figure 9. A1/A2 discrimination diagrams of Hailesitai granites. The original plot is from Eby (1992). (a) Nb-Y-Ce diagram; (b) Nb-Y-3*Ga diagram.

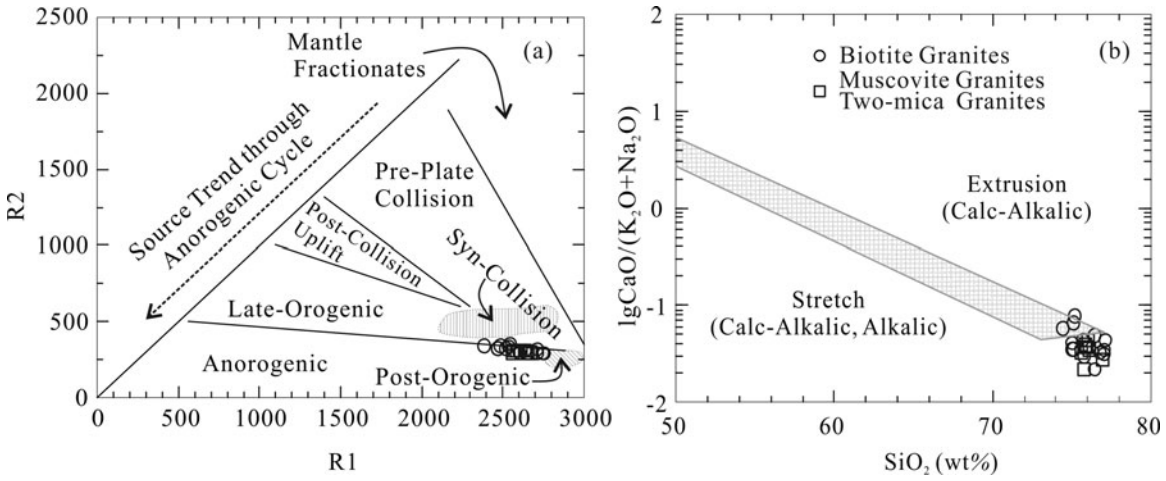

Figure 10. Tectonic discrimination diagrams of Hailesitai granites. (a) R1 versus R2 is after Batchelor & Bowden (1985), R1 = 4Si − 11(Na + K) − 2(Fe + Ti), R2 = 6Ca + 2Mg + Al, molecular ratio; (b) lgCaO/($K_2O + Na_2O$) versus Si_2O is from Allègre & Minster (1978).

https://doi.org/10.1017/S0016756816000534 Published online by Cambridge University Press

much longer than the normal period of magmatic activity associated with a mantle plume (Larson & Olson, 1991; Maruyama, Santosh & Zhao, 2007). Therefore, the Hailesitai pluton might not have been generated under a mantle-plume environment.

A second model suggests that the Mesozoic granite rocks formed because of the subduction of the Mongol–Okhotsk Ocean and subsequent orogenic collapse (Fan *et al.* 2003; Wang *et al.* 2006). Although it might be argued that the Jurassic basalt, exposed in western parts of the GKR, might be related to such subduction and closure of the Mongol–Okhotsk Ocean, the following lines of evidence do not support this interpretation. The Mongol–Okhotsk Ocean subducted northward beneath the Siberia Block and did not subduct southward beneath the GKR, as is required in this model (Sun *et al.* 2013; Tang *et al.* 2013). However, according to available seismic tomography data (Meng, 2003), the Mongol–Okhotsk Ocean subducted southward beneath the GKR. This means that the Mesozoic granitic rocks in the GKR could not have been formed only by subduction of the Mongol–Okhotsk Ocean, because these rocks are distributed not only in the GKR of China but also in eastern Mongolia and Russia (Graham *et al.* 2001). Furthermore, if rocks in the GKR are considered to be the products of post-orogenic evolution, it is difficult to explain why they extend not in a WE direction but in a NNE direction, which parallels the Mongol–Okhotsk Ocean suture (Li *et al.* 2005). Moreover, coeval Mesozoic granitic rocks are widely distributed within the main continental area of eastern China, which cannot be explained only based on the collapse of the Mongol–Okhotsk Orogen (Fig. 1b). The Erguna block has lower $\varepsilon_{Hf}(t)$ values, from −9.7 to +2.5, and higher Nd model ages from 1800 to 1200 Ma, whereas the GKR block has higher $\varepsilon_{Hf}(t)$ values, from +0.6 to +14.16, and lower Nd model ages from 1000 to 500 Ma (Zhang *et al.* 2013; Table 1; Fig. 7b). The Hailesitai granite $\varepsilon_{Hf}(t)$ values (average +11.1; Table 3) are similar to those of the GKR block (Fig. 7b). Higher $\varepsilon_{Hf}(t)$ values and lower Hf second-stage model ages compared to the Erguna block suggest that the period of continental crust growth of the GKR is latter. Furthermore, Siberia subduct south down the Palaeo-Asia Ocean and Mongol–Okhotsk (M-O) belt (Fig. 1). The M-O belt may have enhanced the fertility of the magmatic source areas in NE China.

The third model that has been proposed involves the subduction of the Palaeo-Pacific Plate beneath eastern China (Wang *et al.* 2006), and several lines of evidence support this interpretation. Firstly, the Mesozoic granitic rocks in NE China and the surrounding areas are distributed in a NNE direction, which parallels the NNE-oriented Asian continental margin. Secondly, the geophysical data indicate the existence of a high-velocity zone beneath eastern China, which is commonly considered to be the result of subducted oceanic crust (Huang & Zhao, 2006). Thirdly, it has been documented that Jurassic–Cretaceous accretionary complexes are extensively developed along the entire Asian continental margin, undoubtedly indicating a subduction regime related to the Palaeo-Pacific Plate (Wu *et al.* 2007). However, the following lines of evidence do not support this interpretation. Firstly, the last suture between the northern and southern GKR is the Hegenshan suture zone (Ren, Niu & Liu, 1999), which is located to the east of Hailesitai pluton. Moreover, the formation age of the Mongol–Okhotsk Ocean suture is *c.* 170 Ma at latest (Tomurtogoo *et al.* 2005). This implies that granites older than *c.* 170 Ma and west of the suture in the GKR are mainly affected by the subduction of the Mongol–Okhotsk. This hypothesis is supported by the distribution of the Itype granites aged from 156 to 195 Ma in the Chabaqi area of the GKR (Dai *et al.* 2013). Thus, the Hailesitai pluton might be not the product of the subduction of the Palaeo-Pacific Plate beneath eastern China. Furthermore, the direction shift of the Pacific plate subduction and the regional tectonic setting transfers from the extrusion to the extension is at the Late Jurassic (~145 Ma) in the GKR (Sagong, Kwon & Ree, 2005; Maruyama *et al.* 2006) at latest. In other words, the intrusion age of the A1-type granite in the GKR, which is mainly affected by the subduction of the Pacific Ocean, will not exceed ~145 Ma, and this makes it difficult to explain the intrusion age (~152 and ~161 Ma) of A1-type Hailesitai granites. Eby (1990, 1992) has discussed the fact that the A1-type granite occurred in an intraplate anorogenic rift, post-collisional magmatism, or mantle-plume environment. In the tectonic-setting discrimination diagrams, the Hailesitai granites display the characteristics of an an orogenic environment (Fig. 11). From the Late Jurassic to Early Cretaceous, the granitoids evolved compositionally from highly fractionated I-, transitional I-A or A-type (Wang *et al.* 2015). This evolution coincided with a tectonic transition from contractional crustal thickening to extensional thinning. The Hailesitai A1-type granites aged *c.* 161 and 152 Ma suggest that intraplate orogenesis started from *c.* 161 Ma at latest. Therefore, the formation of the Hailesitai pluton might not have been only affected by the western subduction of the Palaeo-Pacific Plate.

On the basis of the above discussion, we postulate that Hailesitai pluton might be related both to the post-collapse of the Mongol–Okhotsk Orogen and to the subduction of the Palaeo-Pacific Plate. Moreover, the Mongol–Okhotsk Orogen plays a more important role in the evolution of the Hailesitai pluton. The Mongol–Okhotsk Ocean (Palaeo-Asian Ocean) had not disappeared until the Late Permian, when intracontinental orogeny was activated (Li, 2006; Chen *et al.* 2014; Eizenhöfer *et al.* 2014) (Fig. 11a). From the Late Triassic (*c.* 230 Ma) to Middle Jurassic (*c.* 170 Ma), the underplating mafic-ultramafic rocks beneath the micro-blocks were weak lithosphere with the existence of partial melt affected by Mongol–Okhotsk. The Orogen tectonic regime and, simultaneously, minor ocean crust material were also involved in magmatism (Chen *et al.* 2014) (Fig. 11b). According to granitoid zircon ages in the GKR and adjacent area, 165–145 Ma is the

https://doi.org/10.1017/S0016756816000534 Published online by Cambridge University Press

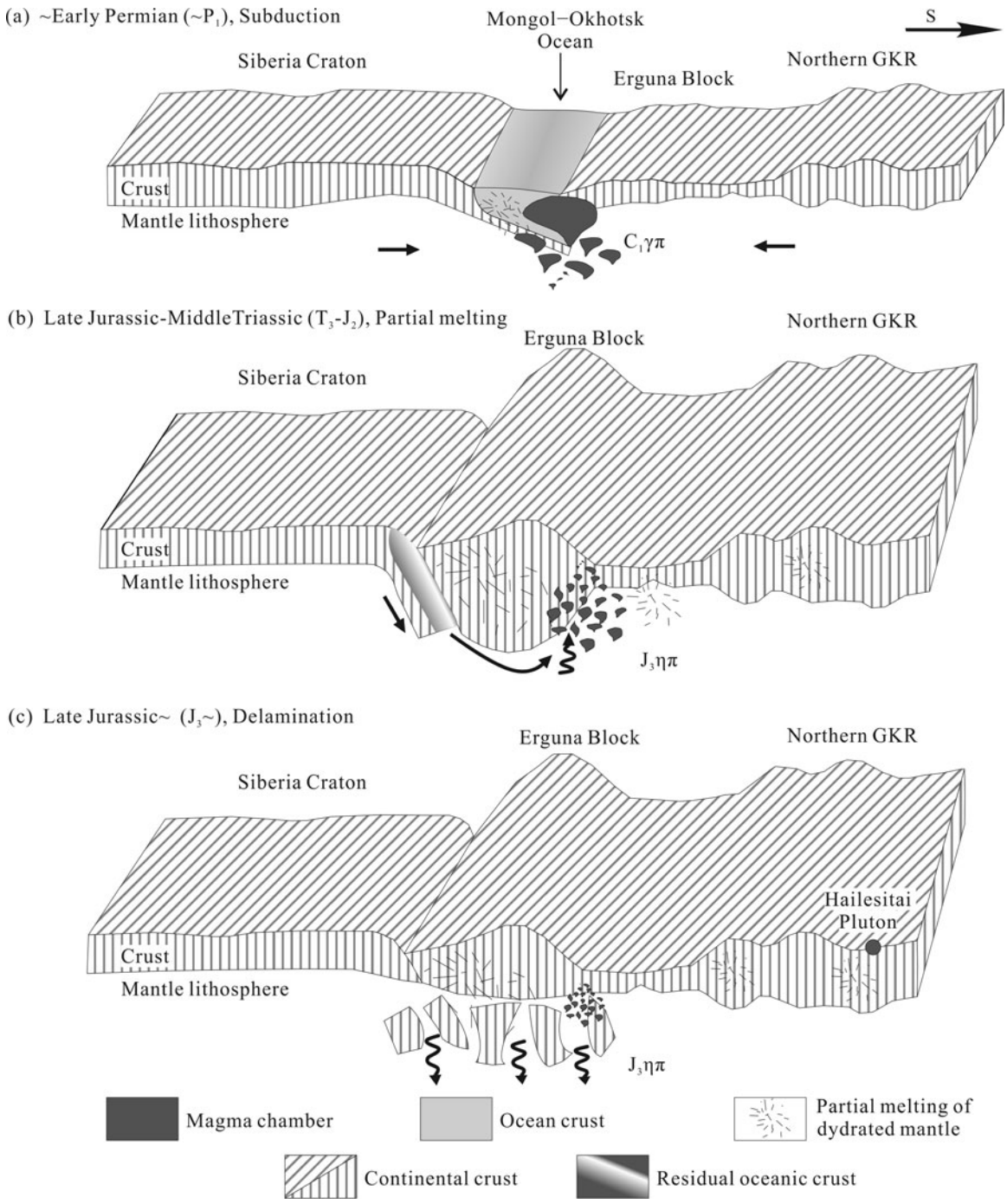

Figure 11. The illustration genesis and dynamics model diagrams of Hailesitai pluton. (a) The Mongol−Okhotsk Ocean (Palaeo-Asian Ocean) subducted southern beneath to the GKR block. (b). The underplating mafic–ultramafic rocks beneath the micro-blocks were weak lithosphere with existence of partial melt affected by Mongol−Okhotsk Orogen tectonic regime, and, simultaneously, minor ocean crust material was also involved in magmatism. Hailesitai granitic magmas generated in basaltic underplating conditions that provide heat and material (=mantle component). Initial basaltic magma was produced by partial melting of mantle peridotites at the lithosphere interface after delamination of the oceanic lithosphere (Jahn, 2004). (c) Delamination of the thick crust, and intraplate evolution was activated.

peak age published (Wang *et al.* 2015). This means that these granitoids might be formed in a delamination setting related to closure of the Mongol−Okhotsk Ocean. At the end of the Late Jurassic, westward flat-slab subduction of the Palaeo-Pacific Oceanic plate changed direction to the N or NW, and this caused a transformation in tectonic regime from compression to extension in the Cretaceous (*c.* 145 Ma) and induced large-scale delamination of the thickened lower crust and lithospheric mantle (Zhang *et al.* 2010). Because of the subduction of the Palaeo-Pacific Plate under the GKR, intercontinental extension occurred in the deep crust (Zhang, Ran & Li, 2012) and the Hailesitai magma chamber was reactivated at the ascent zone (Fig. 11c).

https://doi.org/10.1017/S0016756816000534 Published online by Cambridge University Press

The magma continued to upwell, differentiate and crystallize, and some dehydrated oceanic crust substances, which might have softened the previously thickened lithosphere and resulted in the delamination of the subducted Palaeo-Pacific Plate, were mixed within the upwelling. Therefore, under these circumstances, the coarse-grained A1-type Hailesitai granites could have been formed. And this might be the best model to explain the geochemical characteristics of the Hailesitai pluton.

6. Conclusions

The zircon U−Pb dating and Hf isotope studies for the Hailesitai pluton in the GKR have led to the following conclusions:

(1) The Hailesitai pluton (Late Jurassic coarse granites) was formed in two stages: the earlier stage (*c.* 161 Ma) was formed of biotite granite and the latter stage (*c.* 152 Ma) was formed of biotite and muscovite granites.

(2) The Hailesitai A1-type granitic pluton was sourced from enriched (EM1-type) mantle and a mixture of juvenile and crustal source rocks.

(3) The intra-plate orogenesis of the northern Greater Khingan Range started from *c.* 161 Ma at latest.

(4) The intrusion of the Hailesitai pluton in the GKR formed in response to post-orogenic extensional collapse of the Mongol–Okhotsk belt, coupled with back-arc extension related to Palaeo-Pacific plate subduction.

Acknowledgements. This work was supported by the National Nature Science Foundation of China (NSFC) (4143000344 and 41572315) and the China Geological Survey (12120113056200 and 12120113089000). We thank Lianxun Wang for help with the zircon U−Pb dating and zircon Hf isotope analyses. We are grateful to Nick M.W. Roberts for constructive and helpful reviews and to Mark B. Allen for thoughtful comments on, and editorial handling of, the manuscript.

References

ALLÈGRE, C. J. & MINSTER, J. F. 1978. Quantitative models of trace element behavior in magmatic processes. *Earth and Planetary Science Letters* **38**, 1–25.

ANDERSEN, T. 2002. Correction of common lead in U-Pb analyses that do not report ^{204}Pb. *Chemical Geology* **192**, 59–79.

BARTH, M. G., NOUGH, W. F. & RUDNICK, R. L. 2000. Tracking the budget of Nb and Ta in the continental crust. *Chemical Geology* **165**, 197–213.

BATCHELOR, R. A. & BOWDEN, P. 1985. Petrogenetic interpretation of granitoid rock series using multicationic parameters. *Chemical Geology* **48**, 43–55.

BLICHERT-TOFT, J., CHAUVEL, C. & ALBARÈDE, F. 1997. Separation of Hf and Lu for high-precision isotope analysis of rock samples by magnetic sector-multiple collector ICP-MS. *Contributions to Mineralogy and Petrology* **127**, 248–60.

BONIN, B. 2007. A-type granites and related rocks: evolution of a concept, problems and prospects. *Lithos* **97**, 1–29.

CHEN, Y., LI, D., LIU, C. & LIU, J. 2014. Formation and evolution history of the Da Hinggan Mountains: evidence from geochemistry of rivers' overbank sediments, their zircon U-Pb ages and Hf isotopic compositions. *Acta Geologica Sinica* **88**, 1–14.

COLLINS, W. J., BEAMS, S. D., WHITE, A. J. R. & CHAPPELL, B. W. 1982. Nature and origin of A-type granites with particular reference to southeastern Australia. *Contributions to Mineralogy and Petrology* **80**, 189–200.

CUI, F., ZHENG, C., XU, X., YAO, W., SHI, L., LI, J. & XU, J. 2013. Late Carboniferous magmatic activities in the Quanshenglinchang area, Great Xingan Range: constraints on the timing of amalgamation between Xingan and Songnen Massifs. *Acta Geologica Sinica* **87**, 1247–63 (in Chinese with English abstract).

DAI, H., YANG, Z., MA, Z. & GONG, C. 2013. The petrogeochemical characteristics and tectonic setting of Mesozoic intrusive rocks in Chabaqi area of the Da Hinggan Mountains. *Geologica of China* **40**, 232–47 (in Chinese with English abstract).

EBY, G. N. 1990. The A-type granitoids: a review of their occurrence and chemical characteristics and speculations on their petrogenesis. *Lithos* **26**, 115–34.

EBY, G. N. 1992. Chemical subdivision of the A-type granitoids: petrogenetic and tectonic implications. *Geology* **20**, 641–4.

EIZENHÖFER, P. R., ZHAO, G., ZHANG, J. & SUN, M. 2014. Timing of final closure of the Paleo-Asian Ocean along the Solonker Suture Zone: constraints from the provenance analysis of detrital zircons from Permian sedimentary rocks. *Tectonics* **33**, 441–63.

FAN, W., GUO, F., WANG, Y. & LIN, G. 2003. Late Mesozoic calc-alkaline volcanism of post-orogenic extension in the northern Da Hinggan Mountains, northeastern China. *Journal of Volcanology and Geothermal Research* **121**, 115–35.

FISHER, C. M., VERVOORT, J. D. & HANCHAR, J. M. 2014. Guidelines for reporting zircon Hf isotopic data by LA-MC-ICPMS and potential pitfalls in the interpretation of these data. *Chemical Geology* **363**, 125–33.

FOLAND, K. A. & ALLEN, J. C. 1991. Magma sources for Mesozoic anorogenic granites of the White Mountain magma series, New England, USA. *Contributions to Mineralogy and Petrology* **109**, 195–211.

FROST, B. R., BARNES, C. G., COLLINS, W. J., ARCULUS, R. J., ELLIS, D. J. & FROST, C. D. 2001. A geochemical classification for granitic rocks. *Journal of Petrology* **42**, 2033–48.

FROST, C. D. & FROST, B. R. 2010. On ferroan (A-type) granitoids: their compositional variability and modes of origin. *Journal of Petrology* **52**, 39–53.

GAO, S., ZHANG, B., GU, X., XIE, Q., GAO, C. & GUO, X. 1995. Silurian-Devonian provenance changes of South Qinling basins: implications for accretion of the Yangtze (South China) to the North China cratons. *Tectonophysics* **250**, 183–97.

GE, W., LIN, Q., SUN, D., WU, F. & LI, X. 2000. Geochemical research into origins of two types of Mesozoic rhyolites in Daxing'anling. *Earth Science – Journal of China University of Geosciences* **25**, 172–8 (in Chinese with English abstract).

GE, W., LIN, Q., SUN, D., WU, F., WON, C. K., LEE, M., JIN, M. & YUN, S. 1999. Geochemical characteristics of the Mesozoic basalts in Da Hinggan Ling: evidence of the mantle-crust interaction. *Acta Petrologica Sinica* **15**, 396–407 (in Chinese with English abstract).

GRAHAM, S. A., HENDRIX, M. S., JOHNSON, C. L., BADAMGARAV, D., BADARCH, G., AMORY, J., PORTER, M., BARSBOLD, R., WEBB, L. E. & HACKER, B. R. 2001. Sedimentary record and tectonic implications of

Mesozoic rifting in southeast Mongolia. *Geological Society of America Bulletin* **113**, 1560–79.

GRIFFIN, W. L., PEARSON, N. J., BELOUSOVA, E., JACKSON, S. E., VAN ACHTERBERGH, E., O'REILLY, S. Y. & SHEE, S. R. 2000. The Hf isotope composition of cratonic mantle: LAM-MC-ICPMS analysis of zircon megacrysts in kimberlites. *Geochimica et Cosmochimica Acta* **64**, 133–47.

GUO, F., FAN, W. M., WANG, Y. J. & LIN, G. 2001. Petrogenesis of the late Mesozoic bimodal volcanic rocks in the southern DaHinggan Moutains, China. *Acta Petrologica Sinica* **17**, 161–8 (in Chinese with English abstract).

HOFMANN, A. W. 1986. Nb in Hawaiian magmas: constraints on source composition and evolution. *Chemical Geology* **57**, 17–30.

HORSTWOOD, M. S. A., KOŠLER, J., GEHRELS, G., JACKSON, S. E., MCLEAN, N. M., PATON, C., PEARSON, N. J., SIRCOMBE, K., SYLVESTER, P., VERMEESCH, P., BOWRING, J. F., CONDON, D. J. & SCHOENE, B. 2016. Community-derived standards for LA-ICP-MS U-(Th-)Pb geochronology: uncertainty propagation, age interpretation and data reporting. *Geostandards and Geoanalytical Research*, DOI: 10.1111/j.1751-908X.2016.00379.x.

HUANG, J. & ZHAO, D. 2006. High-resolution mantle tomography of China and surrounding regions. *Journal of Geophysical Solid-Earth Research* **111**, 4813–25 (in Chinese with English abstract).

HUANG, D., ZHU, L., HOU, Q., WANG, J., LIU, J., CHEN, Y., WANG, Z. & LI, D. 2014. Geochemistry of granitoid rocks of Weilasituo Deposit, Inner Mongolia and its tectonic significance. *Geoscience* **28**, 1122–37 (in Chinese with English abstract).

JAHN, B. 2004. The Central Asian Orogenic Belt and growth of the continental crust in the Phanerozoic. In *Aspects of the Tectonic Evolution of China* (eds J. Malpas, C. J. N. Fletcher, J. R. Ali & J. C. Aitcheson), pp. 73–100. Geological Society of London, Special Publication no. 226.

JAHN, B., LITVINOVSKY, B., ZANVILEVICH, A. & REICHOW, M. 2009. Peralkaline granitoid magmatism in the Mongolian-Transbaikalian Belt: evolution, petrogenesis and tectonic significance. *Lithos* **113**, 521–39.

KERR, A. & FRYER, B. J. 1993. Nd isotope evidence for crust-mantle interaction in the generation of A-type granitoid suites in Labrador, Canada. *Chemical Geology* **104**, 39–60.

LARSON, R. L. & OLSON, P. 1991. Mantle plumes control magnetic reversal frequency. *Earth and Planetary Science Letters* **107**, 437–47.

LEI, C. & WANG, X. 2011. Paleogene large-scale volcanism and prospecting implication in the east sag-uplift of Nyanqentanglha arc-back in Tibet, China. *Journal of Chengdu University of Technology* **38**, 571–80 (in Chinese with English abstract).

LI, J. 2006. Permian geodynamic setting of Northeast China and adjacent regions: closure of the Paleo-Asian Ocean and subduction of the Paleo-Pacific Plate. *Journal of Asian Earth Sciences* **26**, 207–24.

LI, Y., LIU, B., ZHAO, H., ZHANG, Y. & HAN, Y. 2005. Mesozoic structural stress field characteristics of the Genghe area of the North Daxinganling. *Geotectonica et Metallogenia* **29**, 443–50 (in Chinese with English abstract).

LIN, Q., GE, W., CAO, L., SUN, D. & LIM, K. 2003. Geochemistry of Mesozoic volcanic rocks in Da Hinggan Ling: the bimodel volcanic rocks. *Geochimica* **32**, 208–22 (in Chinese with English abstract).

LIN, Q., GE, W., SUN, D., WU, F., CHONG, K., KYUNG, D., MYUNG, S., MOON, W., CHI, S. & SUNG, H. 1999. Tectonic significance of Mesozoic volcanic rocks in Northeastern China. *Scientia Geologica Sinica* **33**, 129–39 (in Chinese with English abstract).

LIU, Y., GAO, S., HU, Z., GAO, C., ZONG, K. & WANG, D. 2010. Continental and oceanic crust recycling-induced melt peridotite interactions in the Trans-North China Orogen: U-Pb dating, Hf isotopes and trace elements in zircons from mantle xenoliths. *Journal of Petrology* **51**, 537–71.

LIU, Y., ZONG, K., KELEMEN, P. B. & GAO, S. 2008. Geochemistry and magmatic history of eclogites and ultramafic rocks from the Chinese continental scientific drill hole: subduction and ultrahigh-pressure metamorphism of lower crustal cumulates. *Chemical Geology* **247**, 133–53.

LOISELLE, M. C. & WONES, D. R. 1979. Characteristics and origin of anorogenic granites. *Geological Society of America Abstracts with Programs* **11**, 468.

LUDWIG, K. R. 2009. *Isoplot v. 3.71: A Geochronological Toolkit for Microsoft Excel*. Geochronology Center, Berkeley, Special Publication 4.

MA, C., SHE, Z., XU, P. & WANG, L. 2004. The A-type granite in the southern margin of the Tongbai-Dabie Mountains: evidence from SHRIMP zircon geochronology and petrology geochemistry. *Science in China (D Series: Earth Science)* **34**, 1100–10 (in Chinese with English abstract).

MARUYAMA, S., ISOZAKI, Y., KIMURA, G. & TERABAYASHI, M. 2006. Paleogeographic maps of the Japanese Islands: plate tectonic synthesis from 750 Ma to the present. *Island Arc* **6**, 121–42.

MARUYAMA, S., SANTOSH, M. & ZHAO, D. 2007. Superplume, supercontinent, and post-perovskite: mantle dynamics and anti-plate tectonics on the Core–Mantle Boundary. *Gondwana Research* **11**, 7–37.

MCDONOUGH, W. F. & SUN, S. 1995. The composition of the Earth. *Chemical Geology* **120**, 223–53.

MENG, Q. 2003. What drove late Mesozoic extension of the northern China-Mongolia tract? *Tectonophysics* **369**, 155–74.

MILLER, C. F., MESCHTERWELL, S. & MAPES, R. W. 2003. Hot and cold granites? Implications of zircon saturation temperatures and preservation of inheritance. *Geology* **31**, 529–32.

PEARCE, J. A., HARRIS, N. B. W. & TINDLE, A. G. 1984. Trace element discrimination diagrams for the tectonic interpretation of granitic rocks. *Journal of Petrology* **25**, 956–83.

REN, J., NIU, B. & LIU, Z. 1999. Soft collision, superposition orogeny and polycylic suturing. *Earth Science Frontiers* **6**, 85–93 (in Chinese with English abstract).

SAGONG, H., KWON, S. T. & REE, J. H. 2005. Mesozoic episodic magmatism in South Korea and its tectonic implication. *Tectonics* **24**, 125–7.

SCHERER, E., MUNKER, C. & MEZGER, K. 2001. Calibration of the lutetium-hafnium clock. *Science* **293**, 683–7.

SHAO, J., MU, B., ZHU, H. & ZHANG, L. 2010. Material source and tectonic settings of the Mesozoic mineralization of the DaHinggan Mts. *Acta Petrologica Sinica* **26**, 649–56 (in Chinese with English abstract).

SHAO, J., ZANG, S., MOU, B., LI, X. & WANG, B. 1994. Extensional tectonics and asthenospheric upwelling in the orogenic belt: a case study from Hinggan-Mongolia Orogenic belt. *Chinese Science Bulletin* **39**, 533–7 (in Chinese with English abstract).

SUI, Z., GE, W., XU, X. & ZHANG, J. 2009*a*. Characteristics and geological implications of the Late Paleozoic post-orogenic Shierzhan granite in the Great Xing'an Range. *Acta Petrologica Sinica* **25**, 2679–86 (in Chinese with English abstract).

SUI, Z., GE, W, WU, F. & XU, X. 2009*b*. Hf isotopic characteristics and geological significance of the Chahayan Pluton in Northern Daxing'anling Mountains. *Journal of Jilin University* **39**, 849–56 (in Chinese with English abstract).

SUN, D., GOU, J., WANG, T., REN, Y., LIU, Y., GUO, H., LIU, X. & HU, Z. 2013. Geochronological and geochemical constraints on the Erguna massif basement, NE China: subduction history of the Mongol-Okhotsk oceanic crust. *International Geology Review* **55**, 1801–16.

SUN, W., CHI, X., ZHAO, Z., PAN, S., LIU, J., ZHANG, R. & QUAN, J. 2014. Zircon geochronology constraints on the age and nature of 'Precambrian metamorphic rocks' in the Xing'an block of Northeast China. *International Geology Review* **56**, 672–94.

TANG, J., XU, W. L., WANG, F., WANG, W., XU, M. J. & ZHANG, Y. H. 2013. Geochronology and geochemistry of Neoproterozoic magmatism in the Erguna Massif, NE China: petrogenesis and implications for the breakup of the Rodinia supercontinent. *Precambrian Research* **224**, 597–611.

TOMURTOGOO, O., BADARCH, G., LIU, D., WINDLEY, B. F. & KRÖNER, A. 2005. Zircon age and occurrence of the Adaatsag ophiolite and Muron shear zone, central Mongolia: constraints on the evolution of the Mongol-Okhotsk ocean, suture and orogen. *Journal of the Geological Society* **162**, 125–34.

VOO, R. V. D., SPAKMAN, W. & BIJWAARD, H. 1999. Mesozoicsubducted slabs under Siberia. *Nature* **397**, 246–9.

WANG, F., ZHOU, X., ZHANG, L., YING, J., ZHANG, Y., WU, F. & ZHU, R. 2006. Late Mesozoic volcanism in the Great Xing'an Range (NE China): timing and implications for the dynamic setting of NE Asia. *Earth and Planetary Science Letters* **251**, 179–98.

WANG, P., LIU, W., WANG, S. & SONG, W. 2002. $^{40}Ar/^{39}Ar$ and K/Ar dating on the volcanic rocks in the Songliao basin, NE China: constraints on stratigraphy and basin dynamics. *International Journal of Earth Sciences* **91**, 331–40.

WANG, T., GUO, L., ZHANG, L., YANG, Q., ZHANG, J., TONG, Y. & YE, K. 2015. Timing and evolution of Jurassic-Cretaceous granitoid magmatisms in the Mongol-Okhotsk belt and adjacent areas, NE Asia: implications for transition from contractional crustal thickening to extensional thinning and geodynamic settings. *Journal of Asian Earth Sciences* **97**, 365–92.

WANG, X., XU, Z., LIU, Z. & ZHU, K. 2012. Petrogenesis and tectonic setting of the K-feldspar granites in Chaihe area, central Greater Xing'an Range: constraints from petrogeochemistry and zircon U-Pb isotope chronology. *Acta Petrologica Sinica* **28**, 2647–55 (in Chinese with English abstract).

WANG, Y. & ZHAO, Z. 1997. Geochemistry and origin of the Baerzhe REE-Nb-Be-Zr super-large deposit. *Geochimica* **26**, 24–35 (in Chinese with English abstract).

WHALEN, J. B., CURRIE, K. L. & CHAPPELL, B. W. 1987. A-type granites: geochemical characteristics, discrimination and petrogenesis. *Contributions to Mineralogy & Petrology* **95**, 407–19.

WOODHEAD, J., HERGT, J., SHELLEY, M., EGGINS, S. & KEMP, R. 2004. Zircon Hf-isotope analysis with an excimer laser, depth profiling, ablation of complex geometries, and concomitant age estimation. *Chemical Geology* **209**, 121–35.

WU, F., HAN, R., YANG, J., WILDE, S. A., ZHAI, M. & PARK, S. C. 2007. Initial constraints on the timing of granitic magmatism in North Korea using U–Pb zircon geochronology. *Chemical Geology* **238**, 232–48.

WU, F., JAHN, B. M., WILDE, S. & SUN, D. 2000. Phanerozoic crustal growth: U-Pb and Sr-Nd isotopic evidence from the granites in northeastern China. *Tectonophysics* **328**, 89–113.

WU, F., LIN, J., WILDE, S. A., ZHANG, X. & YANG, J. 2005. Nature and significance of the Early Cretaceous giant igneous event in eastern China. *Earth and Planetary Science Letters* **233**, 103–19.

WU, F., SUN, D., GE, W., ZHANG, Y., GRANT, M. L., WILDE, S. A. & JAHN, B. M. 2011. Geochronology of the Phanerozoic granitoids in northeastern China. *Journal of Asian Earth Sciences* **41**, 1–30.

WU, F., SUN, D., LI, H., JAHN, B. & WILDE, S. 2002. A-type granites in northeastern China: age and geochemical constraints on their petrogenesis. *Chemical Geology* **187**, 143–73.

WU, F., YANG, J., LO, C., WILDE, S. A., SUN, D. & JAHN, B. M. 2007. The Heilongjiang Group: a Jurassic accretionary complex in the Jiamusi Massif at the western Pacific margin of northeastern China. *Island Arc* **16**, 156–72.

YUAN, H., GAO, S., DAI, M., ZONG, C., GÜNTHER, D., FONTAINE, G., LIU, X. & DIWU, C. 2008. Simultaneous determinations of U–Pb age, Hf isotopes and trace element compositions of zircon by excimer laser-ablation quadrupole and multiple-collector ICP-MS. *Chemical Geology* **247**, 100–18.

ZHANG, C., HOLTZ, F., KOEPKE, J., BERNDT, J. & MA, C. 2014. Decompressional anatexis in the migmatite core complex of northern Dabie orogen, eastern China: petrological evidence and Ti-in-quartz thermobarometry. *Lithos* **202**, 227–36.

ZHANG, D., WEI, J., FU, L., CHEN, H., TAN, J., LI, Y., SHI, W. & TIAN, N. 2015. Formation of the Jurassic Changboshan-Xieniqishan highly fractionated I-type granites, northeastern China: implication for the partial melting of juvenile crust induced by asthenospheric mantle upwelling. *Geological Journal* **50**, 122–38.

ZHANG, J., GAO, S., GE, W., WU, F., YANG, J., WILDE, S. A. & LI, M. 2010. Geochronology of the Mesozoic volcanic rocks in the Great Xing'an Range, northeastern China: implications for subduction-induced delamination. *Chemical Geology* **276**, 144–65.

ZHANG, J., GE, W., WU, F. & LIU, X. 2006. Mesozoic bimodal volcanic suite in Zhalantun of the Da Hinggan Range and its geological significance: Zircon U-Pb age and Hf isotopic constraints. *Acta Geologica Sinica (English Edition)* **80**, 58–69.

ZHANG, J., GE, W., WU, F., WILDE, S. A., YANG, J. & LIU, X. 2008. Large-scale Early Cretaceous volcanic events in the northern Great Xing'an Range, Northeastern China. *Lithos* **102**, 138–57.

ZHANG, L., LIU, Y., LI, W., HAN, G., ZHANG, J., ZHAO, Z., JIAN, X. & GUO, Q. 2013. Discussion on the basement properties and east boundary of the Ergun massif. *Scientia Geologica Sinica* **48**, 227–44 (in Chinese with English abstract).

ZHANG, L., ZHOU, X., YING, J., WANG, F., GUO, F., WAN, B. & CHEN, Z. 2008. Geochemistry and Sr-Nd-Pb-Hf isotopes of Early Cretaceous basalts from the Great Xinggan Range, NE China: implications for their origin and mantle source characteristics. *Chemical Geology* **256**, 12–23.

ZHANG, Q., RAN, H. & LI, C. 2012. A-type granite: what is the essence? *Acta Petrologica et Mineralogica* **31**, 621–6 (in Chinese with English abstract).

ZHANG, W., NIE, F., LIU, Y., JIANG, S., XU, H., LAI, X. & PI, X. 2007. Studies on sulfur and lead isotope of the Areheda Pb-Zn-Ag deposit Dong Ujmqin Qi (County), Inner Mongolia. *Journal of Jilin University (Earth Science Edition)* **37**, 868–77 (in Chinese with English abstract).

ZHANG, X., YUAN, L. L., XUE, F., YAN, X. & MAO, Q. 2015. Early Permian A-type granites from central Inner Mongolia, North China: magmatic tracer of post-collisional tectonics and oceanic crustal recycling. *Gondwana Research* **28**, 311–27.

ZHANG, Y., GE, W. & LIU, X. 2008. Isotopic characteristics and its significance of the Xinlin Town pluton, Great Hinggan Mountains. *Journal of Jilin University* **38**, 177–86 (in Chinese with English abstract).

ZHANG, Y., SUN, S. & MAO, Q. 2006. Mesozoic O-type adakitic volcanic rocks and its petrogenesis, paleotectonic dynamic and mineralization significance of the eastern side of southern Da Hinggan, China. *Acta Petrogica Sinica* **22**, 2289–304 (in Chinese with English abstract).

ZHANG, Z., ZUO, R. & CHENG, Q. 2014. The mineralization age of the Makeng Fe deposit, South China: implications from U-Pb and Sm-Nd geochronology. *International Journal of Earth Sciences* **104**, 663–82.

ZHAO, Z., CHI, X., LIU, J., WANG, T. & HU, Z. 2010. Late Paleozoic arc-related magmatism in Yakeshi region,Inner Mongolia: chronological and geochemical evidence. *Acta Petrologica Sinica* **26**, 3245–58 (in Chinese with English abstract).

ZHOU, J., WILDE, S. A., ZHANG, X., REN, S. & ZHENG, C. 2011. Early Paleozoic metamorphic rocks of the Erguna block in the Great Xing'an Range, NE China: evidence for the timing of magmatic and metamorphic events and their tectonic implications. *Tectonophysics* **499**, 105–17.

ZHOU, X., YING, J., ZHANG, L. & ZHANG, Y. 2009. The petrogenesis of Late Mesozoic volcanic rock and the contributions from ancient micro-continents: constraints from the zircon U-Pb dating and Sr-Nd-Pb-Hf isotopic systematics. *Earth Science* **34**, 1–10 (in Chinese with English abstract).

ZHU, H., CHEN, Y., WU, G., LI, Y., ZHANG, Y., WU, T., LIU, Y., WANG, C. & LIU, X. 2013. Zircon U-Pb ages,geochemistry features and its geological implication of Early Cretaceous granites in Xinsheng area of Heihe City. *Global Geology* **32**, 665–80 (in Chinese with English abstract).

https://doi.org/10.1017/S0016756816000534 Published online by Cambridge University Press